IOPscience iopscience.iop.org

Home Search Collections Journals About Contact us My IOPscience

Soft modes and phonon interactions in $Sn_2P_2Se_6$ studied by means of neutron scattering

This article has been downloaded from IOPscience. Please scroll down to see the full text article.

1998 J. Phys.: Condens. Matter 10 4811

(http://iopscience.iop.org/0953-8984/10/22/008)

View the table of contents for this issue, or go to the journal homepage for more

Download details:
IP Address: 171.66.16.209
The article was downloaded on 14/05/2010 at 16:28

Please note that terms and conditions apply.

J. Phys.: Condens. Matter **10** (1998) 4811–4844. Printed in the UK PII: S0953-8984(98)89070-X

Soft modes and phonon interactions in $Sn_2P_2Se_6$ studied by means of neutron scattering

S W H Eijt†, R Currat‡, J E Lorenzo§, P Saint-Grégoire‖, S Katano¶, T Janssen†, B Hennion+ and Yu M Vysochanskii*

† Research Institute for Materials, University of Nijmegen, Toernooiveld, NL-6525 ED Nijmegen, The Netherlands

‡ Institut Laue–Langevin, BP 156X, 38042 Grenoble Cédex, France

§ CNRS Laboratoire de Crystallographie, BP 166, 38042 Grenoble Cédex, France

‖ Université de Toulon-Var, BP 132, 83957 La Garde Cédex, France, and CEMES (UPR CNRS 8011), BP 4347, 31055 Toulouse Cédex, France

¶ Japan Atomic Energy Research Institute, Tokai, Ibaraki 319-11, Japan

+ Laboratoire Léon Brillouin, CE Saclay, 91191 Gif-Sur-Yvette, France

* Institute for Physics and Chemistry of the Solid State, Uzhgorod State University, 294000 Uzhgorod, Ukraine

Received 7 November 1997, in final form 2 March 1998

Abstract. This paper presents an inelastic neutron scattering study of the proper ferroelectric $Sn_2P_2Se_6$ and elastic neutron scattering results on the satellite diffraction pattern which characterizes the modulated phase. The temperature dependences of the satellite intensities and modulation wavevector are in fair agreement with results from previous x-ray experiments. Close to the incommensurate-to-ferroelectric transition temperature T_c, an unexpected intensity overshoot is observed, similar to that seen in birefringence and dilatation experiments.

The relationship between the lattice dynamics and the observed phase transition sequence is examined. The dispersion of the ferroelectric soft optic phonon (P_x-polarization) and of the acoustic phonons is followed along the a^*- and c^*-directions. In the ferroelectric phase, the TO mode shows a considerable softening as the incommensurate phase is approached from below. In the paraelectric ($T > T_i$) and incommensurate ($T_c < T < T_i$) phases, the response from the TO (P_x-polarization) and TA ($\partial u_x/\partial z$ strain) branches has been investigated via a series of constant-q scans in the c^*-direction (approximately the modulation wavevector direction). The combined inelastic line-shapes, as observed in a number of non-equivalent Brillouin zones, could all be analysed in terms of a coupled-mode damped harmonic oscillator model. In addition, a diverging, resolution-limited, central peak is observed close to T_i. It is suggested that the TO–TA coupling lies at the origin of the incommensurate instability. A phenomenological free energy is developed, in the continuum approximation, in which the TO–TA interaction is included via a pseudo-Lifshitz term of the type $(\partial u_x/\partial z)(\partial P_x/\partial z)$.

1. Introduction

Ferroelectric phase transitions have received considerable attention as regards their structural and dynamical aspects—for example, in $BaTiO_3$ [1] and thiourea [2]. In particular, the existence of soft modes and/or order–disorder mechanisms has been the subject of numerous optical and neutron spectroscopic studies. In certain systems, of which the so-called type II incommensurate proper ferroelectrics are examples, an incommensurate (IC) phase appears between the high-temperature (symmetric) phase and the ferroelectric phase. BCCD [3], $NaNO_2$ [4], thiourea [2] and $Sn_2P_2Se_6$ are examples of this class of systems. 'Type II' means

0953-8984/98/224811+34$19.50 © 1998 IOP Publishing Ltd

that the thermodynamic potential contains no Lifshitz invariant. Hence, in such systems the incommensurate phase is thought to arise [5] from the interaction of the ferroelectric soft optic mode with an acoustic mode [3] or with another optic phonon [6], creating an instability at non-zero wavevector.

Electronic mechanisms may also be of importance for the transitions in the semiconductors $Sn_2P_2(S_{1-x}Se_x)_6$. For example, the memory effect [7] observed in the incommensurate phase has been shown to result from the trapping of charge carriers at modulated impurity levels. A similar mechanism is likely to be responsible for the induction by temperature stabilization of an intermediate, probably incommensurate, phase in $Sn_2P_2S_6$, which normally undergoes a direct paraelectric-to-ferroelectric transition. The anomalous intermediate phase is observed when stabilizing the temperature in the paraelectric phase just above the phase transition temperature [8].

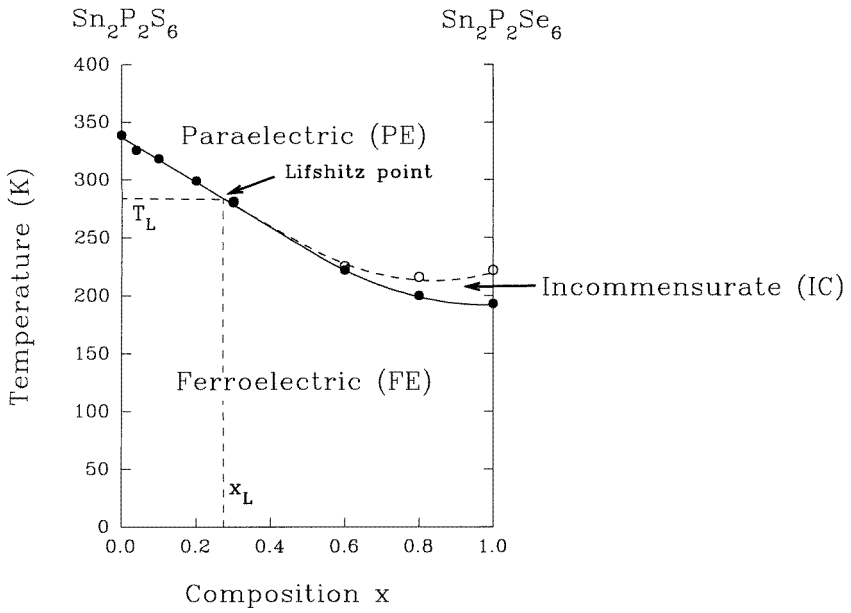

Figure 1. The composition–temperature phase diagram of $Sn_2P_2(S_{1-x}Se_x)_6$ [9].

The $Sn_2P_2(S_{1-x}Se_x)_6$ family of uniaxial ferroelectrics is an excellent model system for studying the appearance of an intermediate IC phase, since mixed crystals can be grown for all values of x $(0 < x < 1)$. $Sn_2P_2Se_6$ shows an intermediate incommensurate phase at ambient pressure, in contrast to $Sn_2P_2S_6$ (figure 1). The latter undergoes a direct second-order phase transition at $T_0 = 337$ K between a paraelectric phase $(P2_1/n)$ and a ferroelectric phase $(Pn; n = (\frac{1}{2}\ 0\ \frac{1}{2})$ for both). The phase transitions in $Sn_2P_2Se_6$ occur at $T_i = 221$ K and $T_c = 193$ K.

The x–T phase diagram exhibits the rare Lifshitz point, at which the period of modulation is expected to become infinite [9]. For crystals with composition $x \leqslant x_L = 0.28$, the phase transition occurs at the Brillouin zone centre $(q = 0)$ and at $q = q_{IC} \neq 0$ for $x \geqslant x_L$. The existence of the Lifshitz point is therefore closely related to the question of why the incommensurate phase exists only in one part of the mixed-crystal (x, T) phase diagram. To gain an understanding on this point we have initiated a lattice dynamical study of the two end members, by means of inelastic neutron scattering, which allows us to probe

phonons throughout the Brillouin zone.

The results of the experiments are reported below. They show the feasibility of further INS studies on mixed crystals, in particular on crystals with x-values close to the 'Lifshitz' composition, where fluctuations will be enhanced. Recent theoretical investigations predict a substantial deviation of the critical exponents from the mean-field value [10] in the vicinity of the multicritical Lifshitz point.

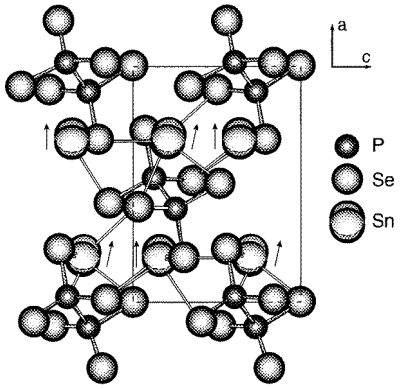

Figure 2. The superimposed structures of $Sn_2P_2Se_6$ in the paraelectric and ferroelectric phases [11, 12], showing the main relative displacements of the Sn^{2+} cations upon transition to the ferroelectric phase (indicated by the arrows).

The changes in structure between the paraelectric and ferroelectric phases have been well studied for $Sn_2P_2Se_6$ [11, 12] and $Sn_2P_2S_6$ [13, 14] via x-ray structure determinations for both phases (figure 2). Throughout the paper we use the pseudo-orthorhombic setting of Rizak *et al* [15]: $a = 9.652$ Å, $b = 7.679$ Å, $c = 6.810$ Å, $\alpha = \gamma = 90^\circ$, $\beta = 91.4^\circ$ ($Sn_2P_2Se_6$, 293 K). The structure includes two $[P_2Se_6]^{4-}$ ionic units, each consisting of two trigonal PSe_3 pyramids, rotated about the connecting phosphor pair. The two $[P_2Se_6]^{4-}$ units are related by a glide plane (an a–c plane) in both phases. In the paraelectric phase, the four tin atoms occupy equivalent general positions and are eightfold coordinated with the selenium atoms. Upon transition to the ferroelectric phase the Sn atoms move in phase, approximately along the a-axis (0.32 Å for Sn(I) and 0.28 Å for Sn(II)) and with opposite phases along the b-axis (0.04 Å) relative to the rigid P_2Se_6 groups, destroying the inversion symmetry and the twofold axis. The displacements correspond to B_u symmetry and result in the appearance of a dielectric polarization in the a–c plane at an angle of 10° to the $\boldsymbol{a}$-axis. In addition, they give rise to two relatively short Sn–Se bonds, leading to the formation of chains of connected P_2Se_6 groups, parallel to the c-axis. $Sn_2P_2S_6$ is isostructural to $Sn_2P_2Se_6$ in both the paraelectric and ferroelectric phases.

The dynamics of the two compounds have been studied both theoretically and experimentally. Some important aspects, such as the mechanism of the incommensurate phase formation, remain unclear however. Lattice dynamical calculations based on a rigid-ion model [15, 16] could simulate a soft B_u phonon in the Brillouin zone centre in the paraelectric phase with ionic displacements mainly along $\boldsymbol{a}$. The soft-mode behaviour of $Sn_2P_2S_6$ has also been studied by Raman [17], infrared [18] and dielectric spectroscopy [19]. The acoustic properties were investigated by means of ultrasound measurements [20, 21] and Brillouin scattering [22]. All of the experimental results indicate that the transition is mainly displacive. In $Sn_2P_2S_6$ the existence of a soft mode in the ferroelectric phase has

clearly been demonstrated by Raman and infrared spectroscopy. The soft mode appears not to soften completely (it is about 0.35 THz at T_0). Infrared measurements for the paraelectric phase of $Sn_2P_2S_6$ indicate an overdamped B_u soft mode at about 0.4 THz, slowly varying with temperature. However, the analysis is difficult due to a strong low-frequency wing partly obscuring the soft-phonon response. The origin of the wing is still unclear and might reflect a coupling of the soft mode to a lower-frequency excitation or an order–disorder component in the neighbourhood of T_0.

Further indications that the soft mode might contain an order–disorder component come from Brillouin scattering, where the LA (u_{zz}) response shows evidence of a coupling to a low-frequency excitation or a central peak close to T_0. Also, specific heat measurements [23] reveal a large transition entropy at the second-order phase transition temperatures T_i (crystals with $x \geqslant x_L$) and T_0 (crystals with $x \leqslant x_L$), typical of an order–disorder transition. In contrast, at the lock-in transition (T_c) a much lower transition entropy was observed.

In this study of $Sn_2P_2Se_6$ it is shown that the harmonic coupling of the soft optic phonon with acoustic and other optic phonons is strong and that a clear soft-mode behaviour is observed in connection with the ferroelectric transition.

In the mixed compounds $Sn_2P_2(S_{1-x}Se_x)_6$, a soft mode in the ferroelectric phase has previously been found in the range $x = 0$ to $x = 0.6$ by Raman spectroscopy [24]. Recently, new Raman experiments have shown that the soft mode can be observed in $Sn_2P_2Se_6$ as well, softening from 1.20 THz to 0.72 THz (at $T_c - 4$ K) [25].

The formation of the incommensurate phase has been simulated in lattice dynamical calculations, which indicated that the rotation of the anions (the P_2Se_6 molecular groups) might contribute to the formation of the incommensurate phase via optic–acoustic mode coupling. The instability was predicted to occur from the coupling of $\partial P_x/\partial y$ and u_{xy}. However, x-ray experiments [26, 27] show that the modulation wavevector of the incommensurate phase points in a direction close to the *c*-axis. Barsamian *et al* [27] found evidence, via x-ray study, that a plane transverse-modulation wave appears in the *a*–*c* glide plane, in which mainly Sn^{2+} cations move by in-phase displacements (in the [0 k 0] planes) approximately along the $\boldsymbol{a}$-direction. The transverse character is not imposed by symmetry, but may be related to the polar character of the displacements.

The Raman investigations by Gommonai *et al* [28] show that the soft mode (in $Sn_2P_2S_6$) has a complicated temperature and directional dependence in the *a*–*c* as well as *a*–*b* planes. There, it could be attributed to strong anisotropic interactions of the soft TO (P_x) mode with the nearby optic modes of P_y- and P_z-polarization, and the LO–TO splitting giving rise to angular dispersion. This poses the further question of whether in the similar compound $Sn_2P_2Se_6$ the incommensurate phase formation is related to an optic–acoustic or to an optic–optic coupling mechanism.

The dynamics in the incommensurate phase, where two new excitation branches (amplitudons and phasons) are expected, has hardly been studied. Dielectric spectroscopy [29] indicates a soft excitation contributing substantially in the 100 GHz range in the paraelectric phase (a soft mode) and incommensurate phase (attributed to the continuation of the paraelectric B_u mode and the (overdamped) phason). However, no direct measurements of these excitations in $Sn_2P_2Se_6$ have yet been performed.

Finally, the exact nature of the lock-in transition is not fully understood. Birefringence, dielectric and dilatation measurements show anomalies in the lower part of the incommensurate phase, indicating that the behaviour of $Sn_2P_2Se_6$ is more complex than is predicted by elementary theoretical models.

All of these open questions motivated the present series of neutron scattering measurements. In section 3 below, the behaviour of the satellite reflections in the incommensurate

phase is reported, while results on the dynamics of $Sn_2P_2Se_6$, with an emphasis on the incommensurate instability, are presented in section 4. The dynamics of $Sn_2P_2S_6$ in both phases will be reported in a subsequent paper [39].

2. Experimental procedure

Two large crystals of $Sn_2P_2Se_6$ (each about 2 cm^3 in volume) were used. Both crystals were grown by the Bridgman technique. The selenium crystals showed metallic reflection, in contrast to the sulphur crystals which are normally optically transparent with a slight pink coloration. The crystalline quality of all of the specimens investigated was found to be adequate by neutron diffraction standards, with no detectable mosaic structure or twinning. One $Sn_2P_2Se_6$ specimen developed cracks after rapid cycling through the first-order lock-in transition at $T_c = 193$ K.

Experiments were carried out on several thermal and cold-source three-axis neutron spectrometers at JAERI-Tokai, Japan (TAS1), LLB-Saclay, France (4F1) and ILL-Grenoble, France (IN3, IN12 and IN14). Several closed-cycle He refrigerators and cryofurnaces were used during the course of the measurements, with typical temperature homogeneity and stability of a fraction of a degree Kelvin.

Inelastic constant-Q measurements were performed in both the energy-gain and energy-loss modes. The instrumental energy resolution was adjusted to match the experimental requirements, by varying the incident- and scattered-neutron energies (from 5 to 14 meV), as well as the neutron beam collimations.

3. The temperature behaviour of the satellite reflections

Measurements of Bragg satellite reflections for the incommensurate phase of $Sn_2P_2Se_6$ were carried out on two samples, sample No 1 and No 2, following previous x-ray diffraction experiments by Barsamian *et al* [26, 27], who reported the satellite wavevector to lie 9° away from the c^*-axis direction. In their second study, Barsamian *et al* [27] found evidence for a (plane) transverse modulation, involving in-phase displacements of the Sn^{2+} cations approximately along the $\boldsymbol{a}$-direction in the [0 1 0] planes. A linear increase of the satellite intensity was found with decreasing temperature.

The dependence of the wavevector on temperature as measured by means of neutron scattering for sample No 1 is given in figure 3 (curve 1). For comparison, the x-ray results have been included. It can be seen that the neutron scattering data for sample No 1 are consistent, well within the error bars, with the most recent x-ray results [27] (curve 4). However, curve 2 (for the neutron study on sample No 2) and 3 (for the x-ray study (1986)) indicate somewhat lower values of q_{c^*} throughout the IC phase. This discrepancy could possibly be of instrumental origin (thermal gradients, inaccurate thermometry) in the case of curve 2, but, nevertheless, the possibility of a small sample dependence cannot be excluded. In the high-temperature part of the IC phase, the wavevector variation is approximately linear in temperature, whereas at lower temperatures a steeper decrease is observed.

The observed temperature dependence of the wavevector has been analysed using a thermodynamical potential of the type [30] (with $\boldsymbol{z}$ along the (fixed) direction of the modulation wavevector $\boldsymbol{q}$):

$$\Phi = \frac{\alpha}{2}P^2 + \frac{\beta}{4}P^4 + \frac{\gamma}{6}P^6 + \frac{\delta'}{2}\left(\frac{\mathrm{d}P}{\mathrm{d}z}\right)^2 + \frac{g}{4}\left(\frac{\mathrm{d}^2P}{\mathrm{d}z^2}\right)^2 + \frac{\lambda}{2}\left(P\frac{\mathrm{d}P}{\mathrm{d}z}\right)^2 \qquad (1)$$

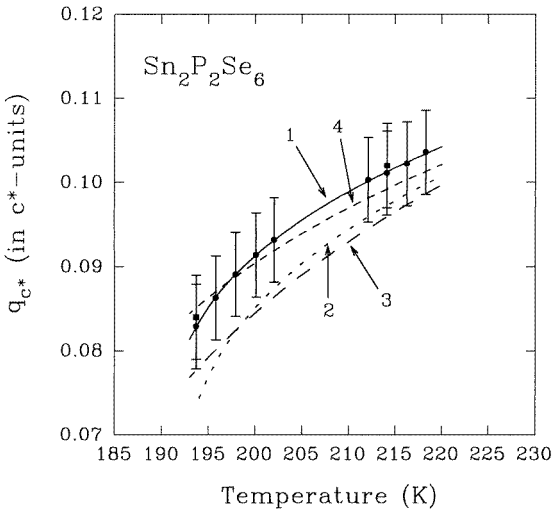

Figure 3. The c^*-component of the modulation wavevector from neutron and x-ray scattering measurements. 1: sample No 1, neutron (this work); 2: sample No 2, neutron (this work); 3: x-ray (1986) [26]; 4: x-ray (1992) [27].

in which $\beta < 0$, $\delta' < 0$, $\gamma > 0$, $g > 0$ and $\lambda > 0$. The coefficient $\beta < 0$, since the virtual paraelectric–ferroelectric transition changes from second order to first order at $x \cong 0.6$ [31]. In this potential the term

$$\frac{\lambda}{2}\left(P\frac{\mathrm{d}P}{\mathrm{d}z}\right)^2$$

is necessary to simulate the change of the modulation wavevector with temperature. Assuming a sinusoidal modulation $\boldsymbol{P} = \boldsymbol{P}_1 \sin(qz)$ and that only $\alpha = a(T - T_0)$ is temperature dependent, it can be shown that [32]

$$q^2(T) = q^2(T_i) + \frac{1}{2}\left(\left(\frac{4\beta_i^2}{9\lambda^2} + \frac{8a}{3g}(T - T_i)\right)^{1/2} - \frac{2\beta_i}{3\lambda}\right) \tag{2}$$

with $\beta_i = \beta + 2\lambda q^2(T_i)$. The coefficient β_i must be positive if we are to obtain a continuous transition at T_i. As a consequence, $2\lambda q^2(T_i) > |\beta|$ should be obeyed.

The experimental curves could all be analysed using formula (2). We performed a weighted averaging on curves 1 and 4 (figure 3) resulting in the values for the thermodynamic potential parameters $2\beta_i/3\lambda$, $8a/3g$ and the magnitude of the modulation wavevector $q(T_i)$, taking the fixed proportionality $q/q_{c^*} \cong 1.014$ into account, given in table 1.

Table 1. Thermodynamic parameters describing the temperature dependence of $q_z(T)$.

$\beta_i/2\lambda$ (in units of $(c^*)^2$)	$8a/3g$ (in units of $(c^*)^2$ K^{-1})	$q(T_i)$ $(=\sqrt{\delta'/2g})$ (in units of c^*)
0.0151 ± 0.0010	$(5.9 \pm 0.5) \times 10^{-6}$	0.1045 ± 0.0005

The direction of the modulation wavevector was checked and found to be constant in the IC phase [26, 27]: the angle that the modulation wavevector makes with the c^*-

axis is found to be $9.4^\circ \pm 0.5^\circ$, in agreement with the x-ray results. We could further confirm the striking invariance of the magnitude of the lattice parameter a in the IC phase: $a = 9.6275 \pm 0.0010$ Å throughout the incommensurate phase.

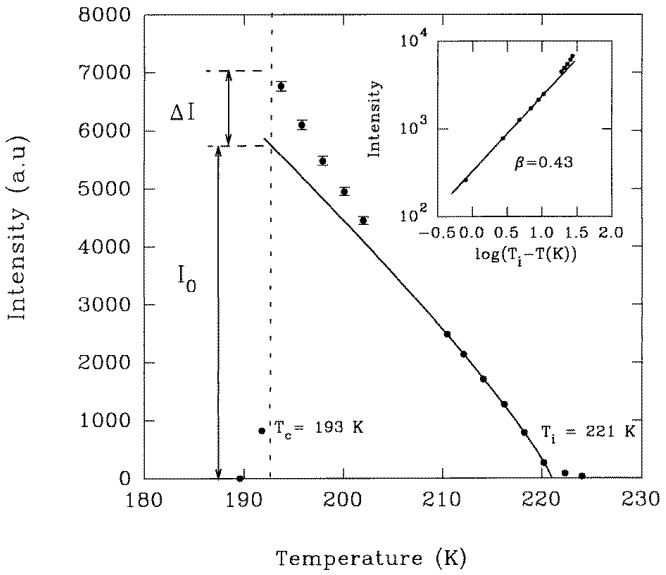

Figure 4. The intensity of the (4 0 0, +) satellite reflection for the incommensurate phase of $Sn_2P_2Se_6$, showing a power-law variation close to T_i with an intensity overshoot ΔI close to the lock-in transition. Inset: determination of the (critical) exponent β.

The integrated intensity $I(T)$ of the (4 0 0, +) = $(4 - q_{a^*}\ 0\ q_{c^*})$ satellite increases monotonically across the IC phase (figure 4). The intensity can be described by a power law at temperatures close to that of the incommensurate phase transition [31]:

$$I(T) = A|T_i - T|^{2\beta} \tag{3}$$

in which $\beta = 0.43 \pm 0.03$ is the order parameter (critical) exponent and that temperature $T_i = 221.0 \pm 0.5$ K. This value for β is close to the value deduced from birefringence measurements ($\beta = 0.46 \pm 0.02$) [33]. In contrast, a pure mean-field behaviour ($\beta = 0.5$) was found in x-ray experiments [26, 27]. In the neutron measurements a straight line, corresponding to mean-field theory, is significantly outside the error bars.

An estimation of the width of the critical region associated with the incommensurate phase transition has been obtained using the Ginzburg–Levanyuk criterion, which says that the IC phase is critical in a temperature interval of 4 K around T_i [34]. The width of the critical region is here a result of the competition between fluctuations, enhanced by the presence of the Lifshitz point (where $\beta \approx 0.2$) in the x–T diagram, and the long-range dipolar forces, which tend to reduce the fluctuation region [31, 34]. In fact, birefringence measurements [35] give a value of $\beta = 0.35$ for a temperature interval close to T_i for $Sn_2P_2Se_6$, as expected from for example a 3d XY-model. This indicates that it is indeed the case that not the whole of the IC phase is critical in this compound, in contrast to what has been claimed for other materials such as Rb_2ZnBr_4. The observed β-value must therefore be considered as an effective value.

At low temperatures an additional intensity is observed, at variance with the x-ray experimental results [27]. A similar additional intensity was found for sample No 2 as

well as in birefringence and dilatation experiments [36]. The magnitude of the intensity overshoot ΔI, relative to the value extrapolated from the high-temperature range $I_0(T_c)$ ($\Delta I/I_0 = 16 \pm 3\%$ for sample No 1 and $15 \pm 5\%$ for sample No 2), is comparable to what has been found in the dilatation experiment, where $\langle \Delta P^2/P_0^2 \rangle$ is 0.17 and 0.19 for vapour-transport-grown and Bridgman-grown crystals, respectively.

The nature of this increase near T_c is still an open question. Though such a behaviour can be expected for certain parameter values of the thermodynamic potential of type II proper ferroelectrics, as shown by Golovko [37], it was found in a model in which soft solitons lead to a (continuous) second-order phase transition. Clearly, for $Sn_2P_2Se_6$ the lock-in transition is first order. Furthermore, the x-ray studies by Barsamian *et al* indicate that higher-order satellites must be of low intensity ($I_{3q} \leqslant 5\%$ of I_q). One possibility is that a second-order phase transition becomes first order, related to strain coupling [38]. It would be interesting to investigate this possibility theoretically for $Sn_2P_2Se_6$-type crystals, for which the coupling between the modulated polarization P_q and strain u_q is expected to be strong in the incommensurate phase.

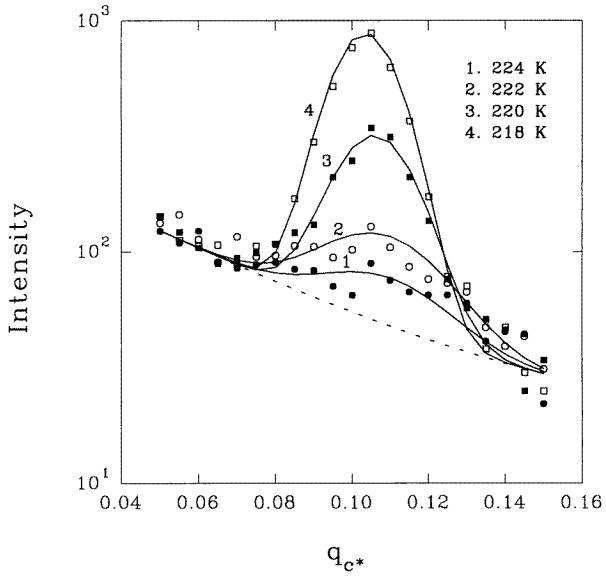

Figure 5. Diffuse scattering along c^* above T_i (curves 1 and 2) and the (4 0 0, +) satellite Bragg reflection below T_i (curves 3 and 4).

The intensity distribution of the diffuse critical scattering has been probed in the paraelectric phase just above T_i using elastic ($E = 0$) scan cross-sections along $\boldsymbol{c}^*$ (figure 5) and $\boldsymbol{a}^*$. In the a^*-direction no significant broadening is observed for the diffuse scattering compared to the satellite peak, as given by Gaussian fits including background. However, along the c^*-direction a clear broadening (65%) can be seen, which survives in the incommensurate phase just below T_i as a weak and broad background (220 K). The difference between the intensity distributions along the a^*- and c^*-directions can be understood, since fluctuations along the ferroelectric axis (at an angle of 10° to $\boldsymbol{a}$) are strongly reduced by dipolar interactions.

Reliable correlation lengths, however, cannot be extracted from our data, since the observed diffuse scattering differs from the total (energy-integrated) diffuse scattering, due

to the finite energy resolution (approximately 0.2 THz). The diffuse intensity observed here arises from the low-frequency part of the acoustic and optic phonon response, as well as from the central peak, close to T_i (see section 4.2).

In figure 5, close to 0.1 c^* a reproducible dip is observed in the diffuse scattering at both 222 K and 224 K. This is characteristic of an interference effect, and might be related to the coupling between the soft TO and the TA phonons in the paraelectric and incommensurate phases, which will be discussed in the next section.

4. The lattice dynamics of $Sn_2P_2Se_6$

The lattice dynamical study of $Sn_2P_2Se_6$ has been carried out on the same two samples, No 1 and No 2, on which the satellite measurements were made. Attention was focused on the low-frequency phonon spectra in the incommensurate and paraelectric phases in order to investigate the soft mode associated with the formation of the incommensurate phase. In addition, we investigated the soft-mode behaviour in the Brillouin zone centre in the ferroelectric phase and its dispersion in the a–c plane at 100 K.

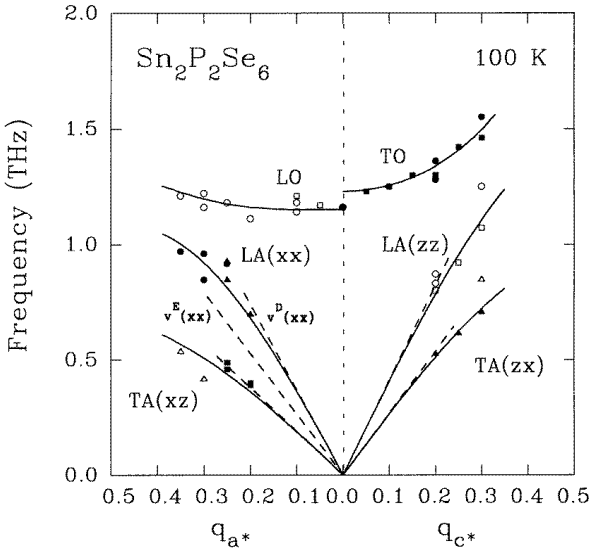

Figure 6. Low-frequency phonon dispersion in the ferroelectric phase of $Sn_2P_2Se_6$. Besides the longitudinal and transverse component of the optic phonon, two LA and TA phonons are observed. Solid lines are guides to the eye. The broken lines are extrapolated from the ultrasonic velocities. The velocity $v^E(xx)$ is obtained by means of ultrasound in the paraelectric phase (see the text); agreement between the slope $v^D(xx)$ and the neutron experiment can be obtained, assuming a value for the electromechanical coupling constant of $k_{11} \approx 0.7$.

4.1. The ferroelectric phase

Figure 6 shows the dispersion of the TA (xz) transverse acoustic phonons as well as the LA (xx) and LA (zz) longitudinal phonons. The limiting slopes of the dispersions, as derived from ultrasound velocity measurements for the ferroelectric phase [21], are given by the dashed lines. A good agreement is observed, except for the LA (xx) branch which deviates from the ultrasonic value of $v^E(xx)$. For the LA (xx) branch, the ultrasonic velocity at

100 K shows a strong dispersion in the frequency range of the measurements (10–70 MHz), which has been attributed to relaxation due to domains. Therefore, the neutron data have been compared to the ultrasonic velocity $v^E(xx)$ obtained in the paraelectric phase, where the domains are absent.

Nevertheless, a discrepancy between the INS and ultrasonic measurements then remains, as seen in figure 6. The same situation is observed for $Sn_2P_2S_6$ [39], for which the discrepancy in $v(xx)$ will be shown to result from an increase in sound velocity caused by the piezoelectric effect, which couples the LA (xx) and LO (P_x) phonons. In this process, the velocity is increased by the additional internal longitudinal electric polarization of the acoustic phonon. This is a result of the macroscopic electric field E^M, similarly to the LO–TO splitting ($\omega_{LO} > \omega_{TO}$) of long-wavelength polar optic modes. The piezoelectric parameters of $Sn_2P_2Se_6$ are undetermined, but from the neutron measurements a value of $k_{11} \approx 0.7$ for the electromechanical coupling constant may be estimated, which is of the same magnitude as the known value of k_{11} for $Sn_2P_2S_6$. This results in the slope indicated by $v^D(xx)$ in figure 6. The coincidence of the slopes and neutron data for the other acoustic branches shows that the corresponding piezoelectric corrections are small.

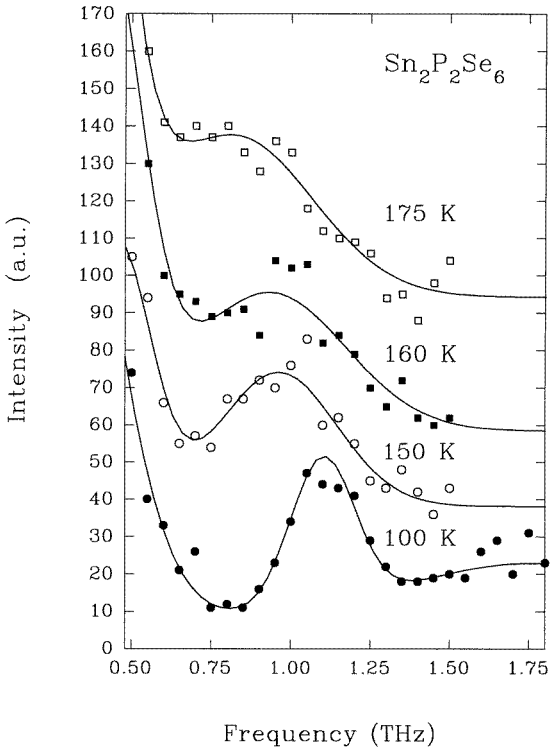

Figure 7. Soft-mode behaviour for the ferroelectric phase of $Sn_2P_2Se_6$ from constant-Q scans at the (3 0 1) Brillouin zone centre. The full lines are damped harmonic oscillator (DHO) fits.

In addition, an x-polarized optic phonon is observed at 1.2 THz at the Brillouin zone centre, in agreement with Raman experiments [40]. The LO–TO splitting is low, about 0.1 THz and, remarkably, negative ($\omega_{LO} < \omega_{TO}$). This is in disagreement with the Raman results, where a small positive splitting of about 0.07 THz is observed. A similar effect is also observed for $Sn_2P_2S_6$ [39]. There it will be shown that the negative splitting for

$Sn_2P_2S_6$ results from coupling to the nearby z-polarized optic phonon. The latter coupling is strong, as observed in Raman experiments. A similar situation is expected to occur for $Sn_2P_2Se_6$.

In figure 7, constant-Q spectra taken at the (3 0 1) zone centre are given for different temperatures for the ferroelectric phase. A clear soft-mode behaviour can be observed: the frequency shows a distinct decrease and the damping increases upon approaching the incommensurate phase transition ($T_c = 193$ K). At low frequencies a strong wing is observed, related to the resolution-broadened Bragg reflection.

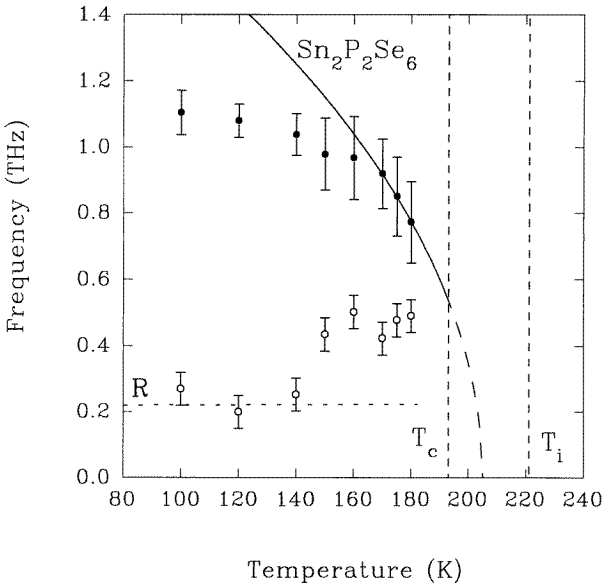

Figure 8. The temperature dependence of the soft-mode frequency (solid circles) and damping (open circles) for the ferroelectric phase of $Sn_2P_2Se_6$. The solid line represents a frequency dependence $\omega^2 = A|T_0 - T|$ with the virtual ferroelectric–paraelectric transition at $T_0 = 205$ K. At low temperature the apparent phonon linewidth is dominated by the resolution R (about 0.22 THz).

The temperature dependence of the SM frequency (figure 8) follows the expected $\omega^2 = A|T_0 - T|$ behaviour close to the lock-in transition, where we used $T_0 = 205$ K for the virtual ferroelectric–paraelectric transition temperature (obtained from an extrapolation of the temperature dependence of the inverse dielectric susceptibility at 10^9 Hz [41]), and $A \approx 0.024$ THz^2 K^{-1}. A much flatter temperature dependence is observed at low temperatures, where the squared frequency clearly does not follow a $\omega^2 = A|T_0 - T|$ law. This behaviour can probably be related to the coupling of the TO (P_x) phonon to other optic phonons, most strongly to the nearby z-polarized optic phonon. The damping shows an increase close to the phase transition, as expected for displacive ferroelectrics [42].

4.2. The paraelectric phase

The observed satellite selection rules confirm the presence of an approximately transverse-modulated ionic displacement wave along $\boldsymbol{q}_{IC}$ (approximately parallel to $\boldsymbol{c}^*$) polarized along $\boldsymbol{a}$, as found previously in x-ray diffraction studies [26, 27]. In order to investigate the temperature behaviour and dispersion of the low-frequency optic and acoustic phonons,

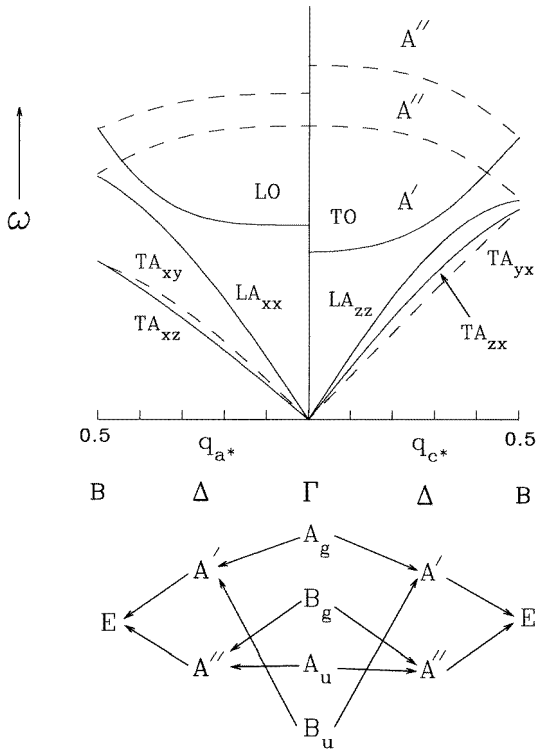

Figure 9. Mode symmetries along the c^*- and a^*-directions in the paraelectric phase ($P2_1/n$). Solid lines represent A′ phonons and dashed lines A″ phonons, respectively.

which are expected to become unstable at T_i, we studied the INS response in several geometries in the a^*–c^* plane with a neutron momentum transfer approximately along $\boldsymbol{a}^*$.

The symmetry of the lattice vibrations in the a–c plane in the paraelectric phase can be determined by correlation methods [43]. The space group $P2_1/n$ ($\boldsymbol{\tau} = (1/2\ 0\ 1/2)$) has four symmetry elements: the glide plane σ normal to [0 1 0] ($\boldsymbol{\tau} = (1/2\ 0\ 1/2)$), the screw axis C_2 ($\boldsymbol{\tau} = (0\ 1/2\ 0)$), the inversion i and the identity E. A schematic picture of the lowest phonon branches in the a^*–c^* directions is given in figure 9. At the zone centre, four different irreducible representations A_g, B_g, A_u and B_u exist. In the a^*–c^* mirror plane (Δ) the modes are symmetric (A′) or anti-symmetric (A″) with respect to the glide plane symmetry. At $\frac{1}{2}\boldsymbol{a}^*$ and $\frac{1}{2}\boldsymbol{c}^*$ the modes are doubly degenerate, because of the non-symmorphicity of the $P2_1/n$ space group which contains a second-order screw axis and a glide plane.

In the Δ plane the possible interactions between phonons of the same representation as the soft P_x-mode (A′) are listed in table 2 below.

In the ferroelectric phase only the glide plane remains. Nevertheless, in the a–c plane

Table 2. Low-frequency modes (A′ symmetry).

Along $\boldsymbol{c}^*$	TA_{zx}	LA_{zz}	TO (P_x)	LO (P_z)
Along $\boldsymbol{a}^*$	TA_{xz}	LA_{xx}	LO (P_x)	TO (P_z)

the same conditions continue to hold, except that at the Γ and B points the irreducible representations change to A′, A″.

In the paraelectric phase, the transverse acoustic TA (u_{xz}) phonon and the low-frequency soft transverse optic TO (P_x) phonon are observed, as both are polarized along $\boldsymbol{a}$. Since the TO and TA phonons are of same symmetry (A′) along $\boldsymbol{c}^*$, the two phonons can be expected to mix (table 2). The TO (P_x) phonon is expected to have a close connection to the IC instability of $Sn_2P_2Se_6$, since in $Sn_2P_2S_6$ the TO (P_x) phonon *is* the soft mode related to the ferroelectric phase, where the spontaneous polarization is approximately directed along $\boldsymbol{a}$.

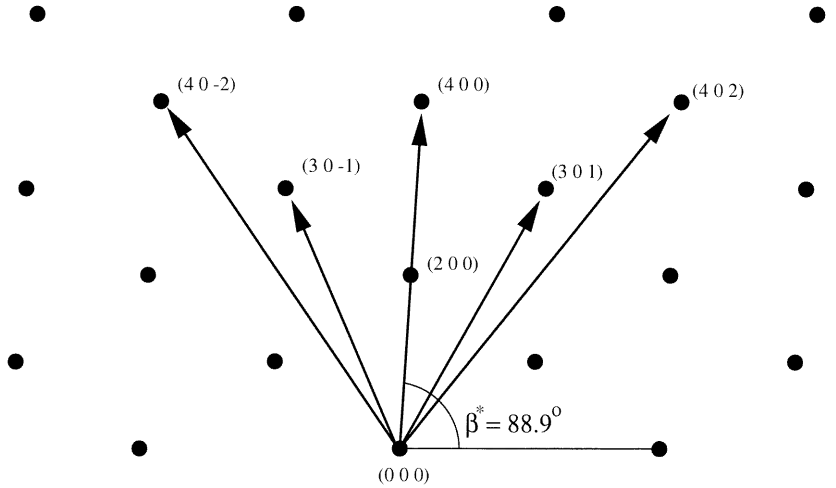

Figure 10. The a^*–c^* scattering plane and the Brillouin zones used in the study of the x-polarized branches.

The study of the temperature behaviour of the low-frequency branches was performed for several Brillouin zones (see figure 10). In these zones the experimental probe is especially sensitive to displacements along $\boldsymbol{a}$ because of the $|\boldsymbol{K}\cdot\boldsymbol{e}|^2$ term in the dynamical structure factor.

First, a study of the dispersion along $\boldsymbol{c}^*$ is presented. Spectra were generally collected at a constant incident-neutron wavevector $k_i = 2.662$ Å^{-1}, yielding a resolution of about 200 GHz. For scans near (3 0 $\pm(1+\xi)$) an incident-neutron wavevector $k_i = 1.64$ Å^{-1} was selected, with an improved energy resolution of about 60 GHz.

In figure 11 we present the spectra obtained in the (3 0 $\pm(1+\xi)$) geometry at 297 K. For the (3 0 $-(1+\xi)$) spectra it seems that only the TA (u_{xz}) phonon is present: the position of the maximum is slightly above the position expected from the value of the sound velocity at room temperature ($v(xz) = 1.83\times10^3$ m s^{-1} at 295 K). The integrated phonon intensity drops as q^2 with increasing q, as is expected for an acoustic phonon with approximately linear dispersion (dashed line).

In the (3 0 $1+\xi$) spectra, at (3 0 1.2) and (3 0 1.3) a second peak is clearly observed at lower frequencies. One of the peaks is approximately at the same position as in the corresponding (3 0 $-(1+\xi)$) scan, albeit slightly displaced to higher frequency: the predicted sound velocity, indicated by the dashed line, corresponds to the lower, relatively sharp edge of the peak rather than to the maximum as for (3 0 −1.3). The lower-frequency peak is assigned to the TO (P_x) phonon branch. It therefore appears that at this temperature and in this wavevector range the TO (P_x) phonon is at lower frequencies than the TA (u_{xz})

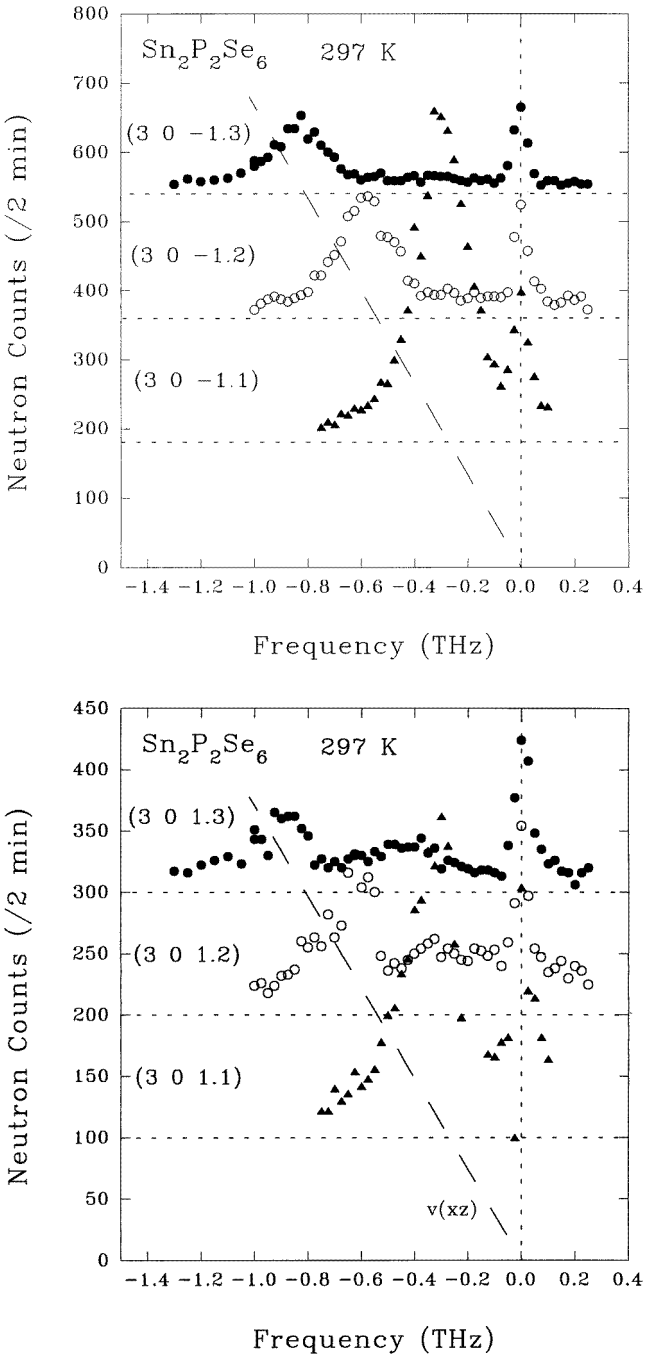

Figure 11. Room temperature spectra at (3 0 $-(1+\xi)$) and at (3 0 $(1+\xi)$). The dashed horizontal lines are shifted baselines.

phonon. It will be shown in section 4.3 how the TA and TO mode frequencies can be extracted from the spectra in figure 11.

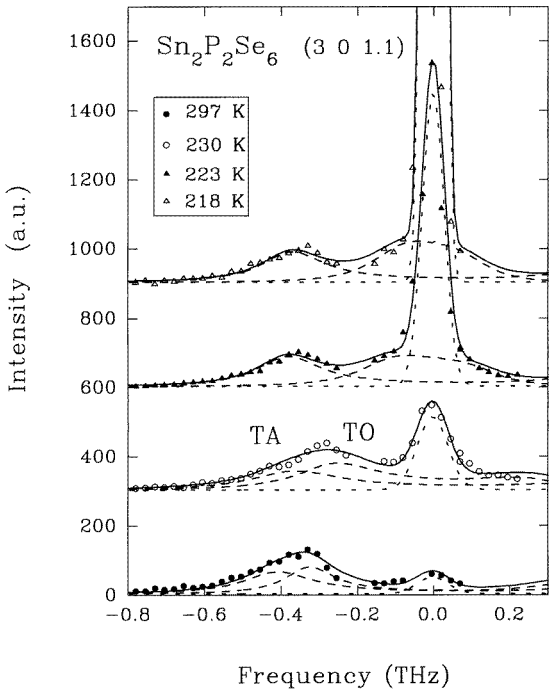

Figure 12. Constant-Q scans at $\boldsymbol{Q}$ = (3 0 1.1) showing the softening of the TO phonon and the appearance of a central peak as $T \rightarrow T_i$.

A clear softening is observed, for example for the spectra at (3 0 1.1), i.e. for a wavevector close to the position of the satellite diffraction peak at $T_i^{(-)}$ (figure 12). The data in the range [−0.26 THz: −0.14 THz] have been removed from the scans in figure 12 because of contamination by the (3 0 1) Bragg tail. Again two phonons are observed in the low-frequency spectra at room temperature, the lowest of which shows a clear soft-mode behaviour on approaching the IC phase transition. Close to T_i, the soft phonon is accompanied by a central peak, which rapidly increases in intensity upon approaching the phase transition and shows a slight narrowing. A damped harmonic oscillator (DHO) analysis clearly shows that the lowest phonon decreases significantly in frequency in the paraelectric phase ($\omega_0 = 0.34$ THz ($\gamma = 0.08$ THz) at 297 K and $\omega_0 = 0.18$ THz ($\gamma = 0.13$ THz) at 223 K), whereas the upper phonon stays more or less at a constant frequency. At 218 K, the strong elastic intensity in figure 12 (top) corresponds to the satellite diffraction peak. A critical elastic component (a 'central peak') is also observed above $T_i = 221$ K, with increasing strength as $T \rightarrow T_i$. At 0.1 $\boldsymbol{c}^*$, this central peak can be detected up to 20 K above T_i. Above 240 K, the elastic intensity at 0.1 $\boldsymbol{c}^*$ is identical to the Q-independent elastic incoherent background. The extent of the central peak in momentum space appears to be quite limited: at 0.2 $\boldsymbol{c}^*$ no extra elastic intensity was detected near T_i. The apparent linewidth of the central component varies from 80 GHz at 230 K and above to 60 GHz at 223 K and below. We believe these widths to be almost entirely of instrumental origin. The apparent frequency narrowing on cooling is probably a consequence of the momentum-space narrowing of the central component on approaching T_i.

The central peak is indicative for an intrinsic order–disorder component in the soft-mode fluctuations. The dynamics is therefore intermediate between those of, for example, $NaNO_2$

(order–disorder) and $SrTiO_3$ (soft mode). In the former, only a central peak is observed, over a wide range of the momentum space, which narrows critically on approaching the phase transition. In the latter, the central peak of unresolved width is believed to be of extrinsic origin, reflecting the coupling between the soft-mode coordinates and slowly relaxing defects or impurities, with a characteristic relaxation rate orders of magnitude slower than that of a typical soft-mode frequency.

The intrinsic character of the central component in $Sn_2P_2Se_6$ is supported by x-ray structural studies and the behaviour of the heat capacity. A recent x-ray structure refinement revealed the partially disordered structure of $Sn_2P_2Se_6$, with two equally occupied (quasi-) equilibrium positions for each tin atom. The heat capacity data revealed a large transition entropy at T_i, characteristic of an order–disorder mechanism in the phase transition. The apparent width of the central peak observed in the neutron study shows that the timescale of the relaxation is at least larger than $\tau \approx 2.5$ ps (0.07 THz), i.e. significantly longer than that of the soft mode (0.18 THz). Interestingly, a Brillouin study of the related crystal $Sn_2P_2S_6$ shows indications for a central peak near its paraelectric–ferroelectric transition.

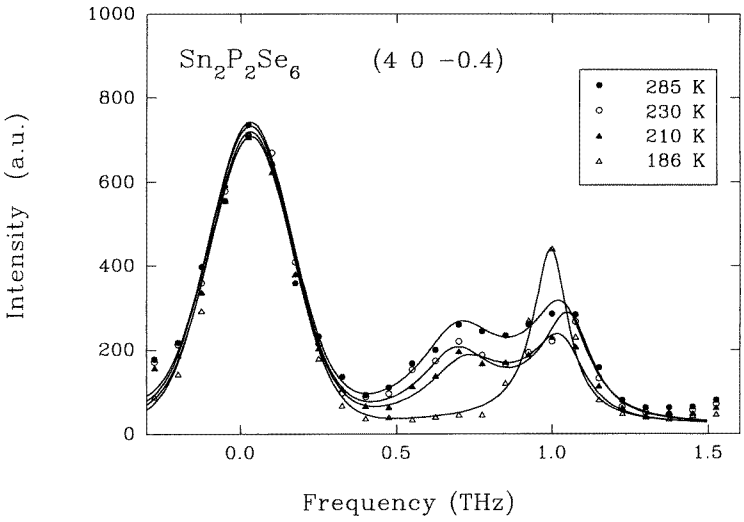

Figure 13. The low-frequency dynamics at (4 0 −0.4). The solid lines are best fits of the spectra according to the coupled-DHO model for the phonons, above T_c (see section 4.3).

4.3. Coupled-mode analysis

We shall now show that the scheme of a low-lying transverse optic ('ferroelectric') branch which softens in the paraelectric phase and which condenses at T_i ($\boldsymbol{q} = 0.1\ \boldsymbol{c}^*$) is oversimplified. In the paraelectric and also in the incommensurate phase it was found that the line-shape strongly depends on the Brillouin zone investigated, as shown for the (3 0 $\pm(1+\xi)$) spectra at room temperature: the (3 0 $1+\xi$) and (3 0 $-(1+\xi)$) spectra show different line-shapes near the upper frequency maximum. Other anomalies are found in the temperature evolution of the two peaks. For example, in the (4 0 $\pm$0.4) zones (figures 13 and 14) the double-peak structure stays more or less the same in the paraelectric and incommensurate phases, but disappears at T_c where only one maximum remains at an intermediate frequency. Also the spectra at (4 0 2.4) and (4 0 1.6) show that a double-

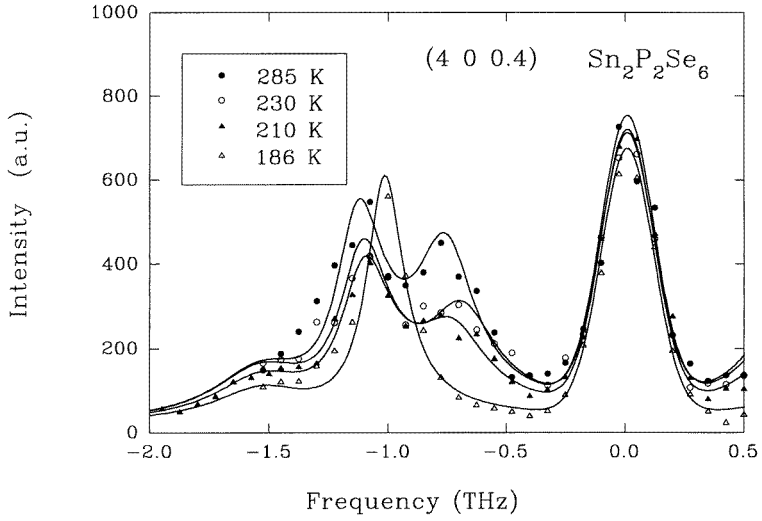

Figure 14. The low-frequency dynamics at (4 0 0.4). The solid lines are best fits of the spectra according to the coupled-DHO model for the phonons, above T_c (see section 4.3), including an additional optic mode at 1.5 THz.

maximum structure is present throughout the incommensurate phase and disappears at T_c.

Line-shapes of the kind shown above are characteristic of interference effects for two coupled oscillators, as previously observed, for example, in $BaTiO_3$ [1], $KNbO_3$ [44] and BCCD [45]. Therefore, we investigated in more detail the spectra for $\boldsymbol{Q} = (3\ 0\ 1.3)$ and $\boldsymbol{Q} = (3\ 0\ -1.3)$ at 230 K (figures 15 and 16). Like in the room temperature spectra (figure 11), the $(3\ 0\ -1.3)$ spectrum appears to exhibit only one (TO) phonon mode, whereas the (3 0 1.3) spectrum indicates the presence of two phonons. An analysis using uncoupled damped harmonic oscillators (figure 15) shows that the two sets of parameter values describing the upper mode are mutually inconsistent. The upper phonon is sharper for (3 0 1.3) than for $(3\ 0\ -1.3)$. Furthermore, the sharp dip in the (3 0 1.3) spectrum and the slow decrease of the response above 0.9 THz cannot be reproduced in a satisfactory way in a DHO analysis.

The two line-shapes can be reconciled by using the response from a pair of coupled oscillators, which can be described by a set of coupled equations of motion as first discussed by Barker and Hopfield [46]. Their description is mathematically equivalent to the coupled-DHO (CDHO) response discussed by Wehner and Steigmeier [47], which is reproduced here.

The model is based on a simple extension of the dynamical matrix for two independent harmonic oscillators:

$$\mathbf{D} = \begin{pmatrix} \omega_1^2 & 0 \\ 0 & \omega_2^2 \end{pmatrix}$$

by inclusion of a term describing the interaction between the two oscillators. This is reflected in the structure of the real and imaginary parts of the phonons' self-energy:

$$\boldsymbol{\pi} = \begin{pmatrix} -\mathrm{i}\,2\omega\gamma_1 & 2\sqrt{\omega_1\omega_2}\Delta_{12} - \mathrm{i}\,2\omega\gamma_{12} \\ 2\sqrt{\omega_1\omega_2}\Delta_{12} - \mathrm{i}\,2\omega\gamma_{12} & -\mathrm{i}\,2\omega\gamma_2 \end{pmatrix}$$

in which the damping (diagonal part) is accompanied by real (Δ_{12}) and imaginary (γ_{12}) coupling coefficients.

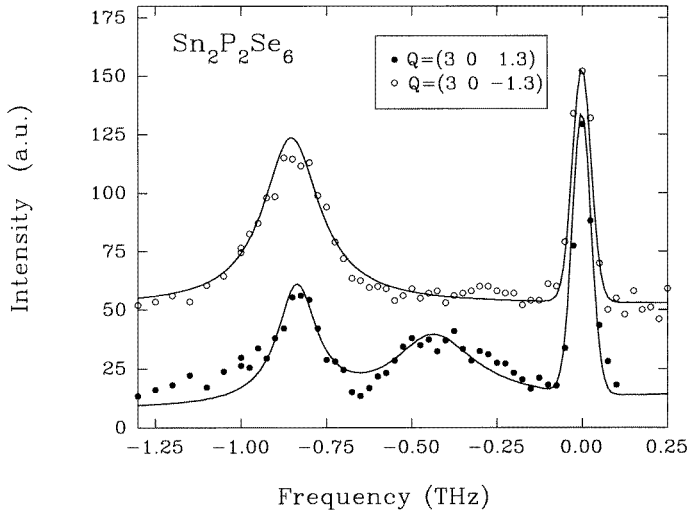

Figure 15. The coupled-mode response in $Sn_2P_2Se_6$ at $\boldsymbol{Q} = (3\ 0\ \pm 1.3)$ and 230 K. The full lines are fits obtained using two independent DHO line-shapes.

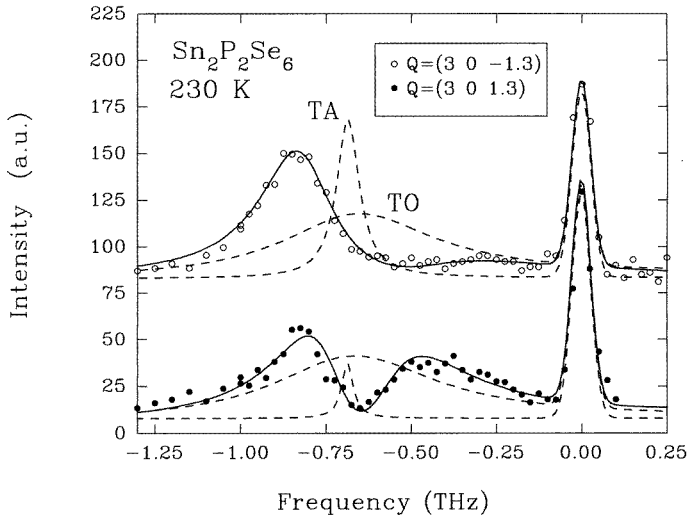

Figure 16. The coupled-mode response in $Sn_2P_2Se_6$ at $\boldsymbol{Q} = (3\ 0\ \pm 1.3)$ and 230 K. The full lines are CDHO fits. The corresponding 'bare' TA and TO phonon response functions are shown as dashed lines.

The response is given by the following equation:

$$J(\omega) = [n(\omega) + 1] \sum_{ik} p_i p_k \,\mathrm{Im}[G_{ik}(\omega)] \tag{4}$$

in which

$$G_{ii}(\omega) = \frac{1}{\omega_i^2 - \omega^2 + \pi_{ii} - \pi_{ik} G_k^{(1)}(\omega) \pi_{ki}} \qquad (k \neq i;\ i, k = 1, 2) \tag{5}$$

$$G_{ik}(\omega) = -G_i^{(1)}(\omega) \pi_{ik} G_{kk}(\omega) \tag{6}$$

$$G_i^{(1)}(\omega) = \frac{1}{\omega_i^2 - \omega^2 + \pi_{ii}}. \tag{7}$$

In these expressions the $G(\omega)$ are the phonon Green functions, determined by the components of the dynamical and self-energy matrices, and the $p_{i,k}$ are the oscillator strengths which reflect the coupling of the oscillators to the experimental probe, in this case the neutron beam. Therefore, p_i and p_k are related to the dynamical structure factors $F_i(K)$ and $F_k(K)$ of the phonons i and k respectively. The expressions for $G_{ik}(\omega)$ satisfy the Dyson equation [47, 48] for the phonon propagators, and include the diagonal and off-diagonal terms, as described by the phonon self-energy terms π_{ik} and π_{ii}, reflecting interactions of the phonons.

It turned out that all of the measured spectra, i.e. at (3 0 $\pm(1+q_{c^*})$) with $k_i = 1.64$ Å^{-1} and at (4 0 $\pm q_{c^*}$), (4 0 2 + q_{c^*}) with $k_i = 2.662$ Å^{-1} could be analysed satisfactorily using the above model, in which we included the $k_f^3 \cot(\theta_f)$ instrumental correction. Consistent oscillator parameters for all of the different zones were obtained (table 3, column 1). For example, in figure 16 the best-fit model simulation for (3 0 ±1.3) is given by the solid lines. Figure 16 shows that the sharp dip for (3 0 1.3) and asymmetric line-shapes are much better recovered using coupled oscillators.

Table 3. Coupled-DHO parameters at 230 K for (3 0 ±1.3). ($\omega_{1,2}$, $\gamma_{1,2}$, Δ_{12}, γ_{12} in THz and p_1, p_2 in arbitrary units.)

	1. Real coupling		2. Imaginary coupling	
	(3 0 −1.3)	(3 0 1.3)	(3 0 −1.3)	(3 0 1.3)
ω_1	0.72	0.71	0.477	0.510
γ_1	0.04	0.02	0.165	0.151
ω_2	0.69	0.72	0.874	0.866
γ_2	0.27	0.29	0.145	0.159
Δ_{12}	0.20	0.19	0.00	0.00
γ_{12}	0.00	0.00	−0.116	−0.136
$p_1 = \|F_1\|$	0.30	0.13	−0.106	−0.219
$p_2 = \|F_2\|$	0.42	0.45	0.50	0.417

In figure 16 the 'bare' uncoupled phonons (dashed lines) are shown, obtained by setting the interaction to zero: Δ_{12}, $\gamma_{12} = 0$. The analysis suggests that the damped soft TO (P_x) phonon (oscillator 2) overlaps with the neighbouring sharp TA (u_{xz}) phonon (oscillator 1). The coupling is quite strong, as is reflected in the prominent distortions of the uncoupled line-shape and the large value of Δ_{12}. For example, in the (3 0 ±1.3) spectra at 230 K, Δ_{12} is roughly 50% of $\sqrt{\omega_1\omega_2}/2$, which is the upper physical limit for Δ_{12} (consistent with the requirement of real diagonalized frequencies (see [46])).

It should be noted that the difference between the spectra at $\boldsymbol{Q}$ = (3 0 1.3) and $\boldsymbol{Q}$ = (3 0 −1.3) arises entirely from the variation of p_1, the bare acoustic mode structure factor. In table 4 the best-fit parameters are shown for all of the spectra measured at 230 K. It is seen that the line-shape changes in the (3 0 $\pm(1+q_{c^*})$) spectra arise from the fact that the structure factor of the 'acoustic' mode is low for (3 0 $1+q_{c^*}$) and high for (3 0 $-(1+q_{c^*})$), whereas the optic mode is more or less the same for both. The sharpest features (e.g. the dip at 0.7 THz) are clearly wider than the energy resolution of 0.06 THz. This shows that the spectra taken at $k_i = 1.64$ Å^{-1} may be used to obtain physically meaningful damping parameter values ($\gamma_{1,2}$ in table 4). In contrast, the values for the dampings obtained at 0.4 $\boldsymbol{c}^*$ are unreliable due to the lower resolution at $k_i = 2.662$ Å^{-1} and have been left out. The

Table 4. Parameters for coupled damped harmonic phonons at 230 K. ($\omega_{1,2}$, $\gamma_{1,2}$, Δ_{12}, γ_{12} in THz and F_1, F_2 in arbitrary units.)

Q	$\lvert F_1(\boldsymbol{Q})\rvert$	$\lvert F_2(\boldsymbol{Q})\rvert$	Δ_{12}	γ_{12}	ω_1	ω_2	γ_1	γ_2
(3 0 −1.1)	0.48	0.52	0.075	0.00	0.23	0.30	0.07	0.24
(3 0 1.1)	0.41	0.73	0.08	0.00	0.22	0.29	0.03	0.22
(3 0 −1.2)	0.40	0.54	0.16	0.00	0.52	0.47	0.06	0.28
(3 0 1.2)	0.17	0.45	0.17	0.00	0.48	0.47	0.03	0.26
(3 0 −1.3)	0.30	0.42	0.20	0.00	0.72	0.69	0.04	0.27
(3 0 1.3)	0.13	0.45	0.19	0.00	0.71	0.72	0.02	0.29
(4 0 −0.4)	1.89	0.00	0.17	0.00	0.98	0.85		
(4 0 0.4)	2.20	0.00	0.18	0.00	1.04	0.83		
(4 0 1.6)	0.087	1.64	0.16	0.00	1.04	0.82		
(4 0 2.4)	1.53	0.00	0.13	0.00	1.01	0.82		

parameter values at 0.4 $\boldsymbol{c}^*$ show further a somewhat larger spread than those for (3 0 ±1.1), (3 0 ±1.2) and (3 0 ±1.3).

The spectra at (4 0 2) and (4 0 0) for $\boldsymbol{q}_{c^*} = \pm 0.4\ \boldsymbol{c}^*$ have been analysed in the CDHO model as well, resulting in fits which are in good agreement with the data (figures 13, 14). In figure 17 the spectra and fits for (4 0 2.4) are plotted at various temperatures. The (4 0 2.4) spectrum has two maxima below 1.2 THz: a dominating sharp high-frequency maximum at 1.05 THz and a weak broad shoulder at around 0.7 THz. On the other hand, at (4 0 1.6) the broad low-frequency maximum at about 0.7 THz is dominant. The difference is reflected in the parameters of the analysis (table 4), which show that the (4 0 2.4) spectrum is produced by phonon 1 (acoustic) only, while the (4 0 1.6) spectrum consists mainly of the optic contribution (phonon 2).

It is interesting to note that, even if the intensity of phonon 2 is negligible (as for example at (4 0 0.4), table 4), the frequency and damping of *both* modes can be extracted from the distorted line-shape. This reflects the fact that the response from the two phonons cannot be reduced to a sum of the response functions from two independent renormalized modes. This can be seen also in the equations given by Barker and Hopfield, which cannot be transformed into two separate equations describing two independent DHOs. It shows that (thermal) excitation of the acoustic phonon leads to an (indirect) response at the 'optic' frequency.

4.4. Discussion

In the above-described analysis, a satisfactory agreement with all of the measured spectra has been obtained using a real coupling for all of the spectra. Further on, the assumption of real coupling will be shown to be consistent with a continuum model for the thermodynamic potential for the paraelectric phase of $Sn_2P_2Se_6$. Important to notice, however, is the fact that in the CDHO model one (real) parameter may be chosen arbitrarily, producing an infinite number of equivalent parameter sets corresponding to the same calculated response function, as shown by Barker and Hopfield [46].

In inelastic neutron scattering by two coupled phonons, the equation for the inelastic scattering law $S(\boldsymbol{K}, \omega)$ is different from that for $J(\omega)$, equation (4), in the eight-parameter model, since the coupling of phonons to the experimental probe is different to that in the case of light scattering. Therefore, neutron scattering may in principle provide an opportunity to lift this indeterminacy, and determine the relative phase of the $F_j(\boldsymbol{K})$, as was done partially

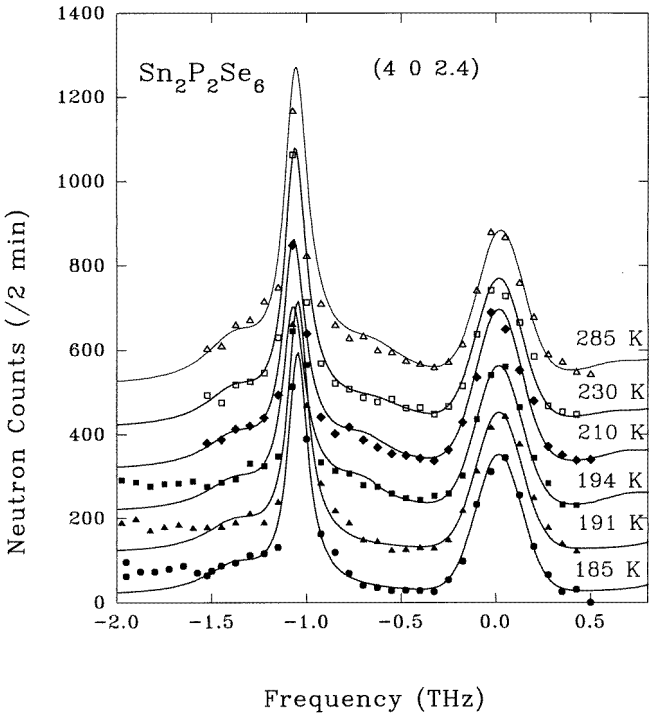

Figure 17. The low-frequency dynamics at (4 0 2.4) at various temperatures. Above T_c a broad wing is observed below the sharp maximum at around 1.0 THz, which suddenly disappears at T_c (as explained in section 4.6). The CDHO dynamics below 1.2 THz is accompanied by higher-frequency optic phonons. The solid lines are fits according to the CDHO model ($T > T_c$) and a DHO model ($T < T_c$).

for the case of cubic $BaTiO_3$ [1]. The inelastic scattering law $S(\boldsymbol{K}, \omega)$ can be expressed in terms of the phonon coordinates $Q(\boldsymbol{q}j)$ and $Q(\boldsymbol{q}j')$ of the coupled branches j and j', with $\boldsymbol{K} = \boldsymbol{\tau} + \boldsymbol{q}$ ($\boldsymbol{\tau} \in \Lambda^*$ and $\boldsymbol{q}$ is a vector in the Brillouin zone):

$$S(\boldsymbol{K}, \omega) = \sum_{j,j'} F_j(\boldsymbol{K}) F_{j'}^*(\boldsymbol{K}) \int_{-\infty}^{\infty} \mathrm{d}t \ \mathrm{e}^{-\mathrm{i}\omega t} \langle Q^\dagger(\boldsymbol{q}j, 0) Q(\boldsymbol{q}j', t) \rangle \tag{8}$$

with the phonon structure factor $F(\boldsymbol{K})$ given by

$$F_j(\boldsymbol{K}) = \sum_d b_d \mathrm{e}^{-W_d(\boldsymbol{K},j)} \mathrm{e}^{\mathrm{i}\boldsymbol{K}\cdot\boldsymbol{r}_d} [\boldsymbol{K} \cdot \boldsymbol{e}_d(\boldsymbol{q}, j)] M_d^{-1/2}. \tag{9}$$

In the case of coupled phonons, terms with $j \neq j'$ appear in equation (8) in addition to the usual individual phonon correlators (polarization mixing). One can show that the scattering law can be written in terms of phonon Green's functions as

$$S(\boldsymbol{K}, \omega) = \sum_{j,j'} F_j(\boldsymbol{K}) F_{j'}^*(\boldsymbol{K}) [n(\omega) + 1] \, \mathrm{Im}[G_{jj'}(\omega)] \tag{10}$$

establishing the relation with equation (4). In expression (10) the relative phase of the complex dynamical structure factors $F_j(\boldsymbol{K})$ and $F_{j'}^*(\boldsymbol{K})$ of the two coupled phonons is *not* arbitrary (as would be the case for uncoupled phonons). First, the nature of the coupling (real or imaginary) imposes strict phase relations between the two eigenvectors, $\Delta\phi_{j,j'}^c(\boldsymbol{q})$. Also, the dynamical structure factors are complex because of the various complex terms

in the summation (9) due to the position of the atoms and the size of the eigenvector components. This gives rise to a second phase difference $\Delta\phi^F_{j,j'}(\boldsymbol{K})$, now dependent on the total $\boldsymbol{K}$. Therefore, the phase difference of the complex dynamic structure factors is $\Delta\phi_{1,2}(\boldsymbol{K}) = \Delta\phi^c_{1,2}(\boldsymbol{q}) + \Delta\phi^F_{1,2}(\boldsymbol{K})$. Furthermore, since $G_{12}(\omega) = G_{21}(\omega)$ we arrive at the following relation for two coupled phonons:

$$S(\boldsymbol{K},\omega) = [n(\omega)+1]\Big\{|F_1(\boldsymbol{K})|^2\,\mathrm{Im}[G_{11}(\omega)] + 2\cos(\Delta\phi_{1,2}(\boldsymbol{K}))|F_1(\boldsymbol{K})||F_2(\boldsymbol{K})|\,\mathrm{Im}[G_{12}(\omega)] + |F_2(\boldsymbol{K})|^2\,\mathrm{Im}[G_{22}(\omega)]\Big\}. \tag{11}$$

In equation (11) the coupled phonon propagators G_{ik} are defined according to equations (2)–(4). The additional $\cos(\Delta\phi_{1,2}(\boldsymbol{K}))$ term prevents one from transforming equation (11) into equation (4), upon replacing $|F_i(\boldsymbol{K})|$ by p_i. The actual observed line-shape will therefore differ from $J(\omega)$ by a response proportional to $\mathrm{Im}[G_{12}(\omega)]$. Neutron scattering therefore may offer a way to determine the relative phase of the phonon coupling, by measuring the dynamics at $\boldsymbol{q}$ in several Brillouin zones at $\boldsymbol{K} = \boldsymbol{\tau} + \boldsymbol{q}$.

Nevertheless, such a determination in practice is limited by the few Brillouin zones actually accessible, preventing a rigorous determination of the eigenvectors and the phase $\Delta\phi^F_{1,2}(\boldsymbol{K})$ from being made, as well as the low signal-to-noise ratio, preventing a strict test of the validity of the CDHO model from being carried out.

In our study, only two zones were studied with a sufficient resolution (60 GHz) for each wavevector $\boldsymbol{q}$. Therefore, the (perhaps rather crude) restriction of $\Delta\phi_{1,2}(\boldsymbol{K}) = 0$ was imposed†. It is clear that in the case of $\Delta\phi_{1,2}(\boldsymbol{K}) = 0$ the CDHO model may be applied successfully to describe the observed spectra consistently.

In the eight-parameter model (equivalent to $\Delta\phi_{1,2}(\boldsymbol{K}) = 0$), the choice of real or imaginary coupling is mathematically arbitrary. In what follows, the dispersion branches will be presented using an imaginary coupling, which is equivalent to the case of a diagonalized dynamical matrix $\mathbf{D}$ (section 4.3). The frequencies obtained may in such a case be directly compared to those lattice dynamical calculations which do incorporate the interaction. Moreover, it prevents a non-allowed crossing of branches, which would occur in the analysis of $Sn_2P_2Se_6$ using a purely real coupling.

The analysis involving a purely real coupling, presented before, may be used to obtain the true frequencies, corresponding to uncoupled modes of mixed character, by diagonalizing the dynamical matrix $\mathbf{D}$ including the real part of the interaction:

$$\mathbf{D} = \begin{pmatrix} \omega_1^2 & 2\sqrt{\omega_1\omega_2}\Delta_{12} \\ 2\sqrt{\omega_1\omega_2}\Delta_{12} & \omega_2^2 \end{pmatrix}.$$

The diagonalized frequencies ω_+ and ω_- obey

$$\omega_\pm^2 = \frac{1}{2}(\omega_1^2+\omega_2^2) \pm \frac{1}{2}\sqrt{(\omega_1^2+\omega_2^2)^2 - 4(\omega_1^2\omega_2^2 - 4\omega_1\omega_2\Delta_{12}^2)}. \tag{12}$$

The diagonalization is equivalent to the coordinate transformation $\mathbf{U}$ for (P_x, u_{xz}):

$$\mathbf{U} = \begin{pmatrix} \cos\theta & \sin\theta \\ -\sin\theta & \cos\theta \end{pmatrix}$$

in which

$$\tan 2\theta = \frac{4\sqrt{\omega_1\omega_2}\Delta_{12}}{\omega_1^2 - \omega_2^2}$$

† In fact, calculations show that the exact shape is rather sensitive to the phase (keeping the other parameters fixed), especially when the responses of the two phonons overlap and $|F_1(\boldsymbol{K})| \sim |F_2(\boldsymbol{K})|$.

as discussed by Barker and Hopfield [46]. Table 3 shows an example of two equivalent parameter sets (1 and 2), obtained by diagonalizing parameter set 1. The changes in the two frequencies reveal the repulsion between the two phonons occurring because of the real interaction. The two branches obtained will have a mixed optic–acoustic character, especially at $\boldsymbol{q}$-positions where the interaction is strong and the (bare) frequencies are close.

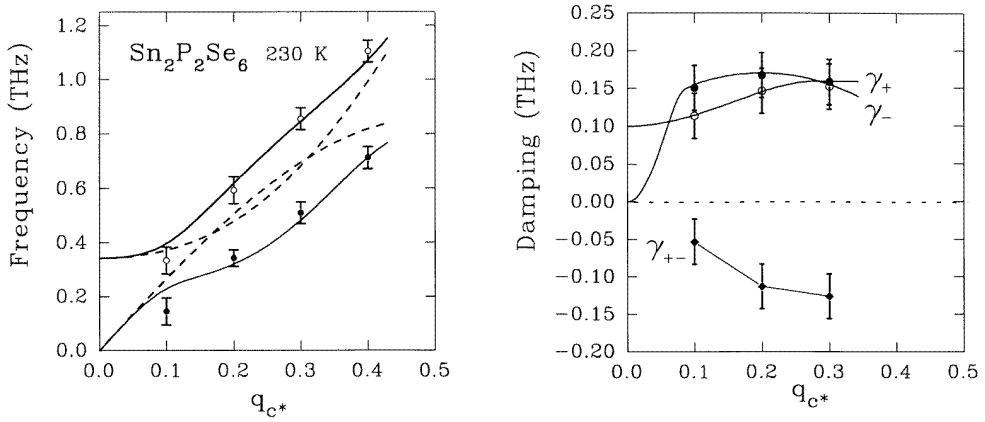

Figure 18. The dispersion at 230.7 K, $\boldsymbol{Q} = (3\ 0\ 1+\xi)$ with diagonalized frequencies (ω_+ and ω_-). The dashed lines are the bare branches in the continuum model (section 4.5), which transform into the full lines on taking the coupling into account. Also, the dampings of the mixed phonons γ_+ and γ_- are presented, together with the interaction damping γ_{+-}.

The diagonalization of the dynamical matrix will be accompanied by a corresponding transformation of the damping matrix $\boldsymbol{\Gamma}' = \mathbf{U}\boldsymbol{\Gamma}\mathbf{U}^\dagger$:

$$\boldsymbol{\Gamma} = \begin{pmatrix} \gamma_1 & \gamma_{12} \\ \gamma_{12} & \gamma_2 \end{pmatrix} = \begin{pmatrix} \gamma_1 & 0 \\ 0 & \gamma_2 \end{pmatrix} \rightarrow \boldsymbol{\Gamma}' = \begin{pmatrix} \gamma_+ & \gamma_{+-} \\ \gamma_{+-} & \gamma_- \end{pmatrix}.$$

After the transformation $\mathbf{U}$, the line-shape distortions are reflected by the non-zero and large γ_{12} (table 3, column 2, and figure 18).

The parameters obtained from the CDHO analysis of the spectra (see section 4.3) for various zones were averaged: the dispersion points at $\boldsymbol{q}_{c^*} = 0.1\ \boldsymbol{c}^*$, $0.2\ \boldsymbol{c}^*$ and $0.3\ \boldsymbol{c}^*$ were obtained at $(3\ 0\ \pm(1+q_{c^*}))$ and at $\boldsymbol{q}_{c^*} = 0.4\ \boldsymbol{c}^*$ they were obtained at $(4\ 0\ \pm q_{c^*})$ and $(4\ 0\ 2 \pm q_{c^*})$. The error bars were determined from the spread in the parameters of the different zones, which were slightly larger than the individual errors of the fits. Subsequently they were converted to the representation with $\Delta_{12} = 0$, $\omega_\pm$ and $\boldsymbol{\Gamma}'$, following the procedure described above. The dispersion branches at 230 K are presented in figure 18, together with the corresponding damping matrix $\boldsymbol{\Gamma}'$ (γ_-, γ_+, γ_{+-}).

It is interesting to notice that the lowest branch is almost at the position of the lowest 'optic' peak and the higher branch is at the position of the higher 'acoustic' maximum of figure 11 for $(3\ 0\ 1+\xi)$ spectra.

Clearly, the two frequencies are temperature dependent (figures 18, 19 and 20). At $0.1\ \boldsymbol{c}^*$, the upper branch softens, whereas at $0.2\ \boldsymbol{c}^*$ the lower branch softens. At higher values of q_{c^*}, the branches are more or less temperature independent. A clear repulsion between the two branches is observed at low q-values, accompanied by a transfer of damping from the upper to the lower branch, most clearly at $0.1\ \boldsymbol{c}^*$. The damping of the upper branch is almost q-independent, whereas the damping of the lower acoustic branch should obey $\gamma_- \propto q^2$ for low q-values.

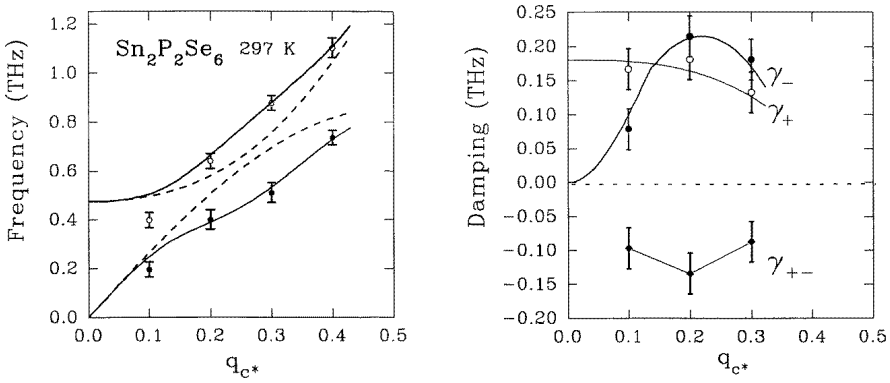

Figure 19. The dispersion at 297 K, $\boldsymbol{Q} = (3\ 0\ 1+\xi)$ with diagonalized frequencies (ω_+ and ω_-). The dashed lines are the bare branches in the continuum model, which transform into the full lines on taking the coupling into account.

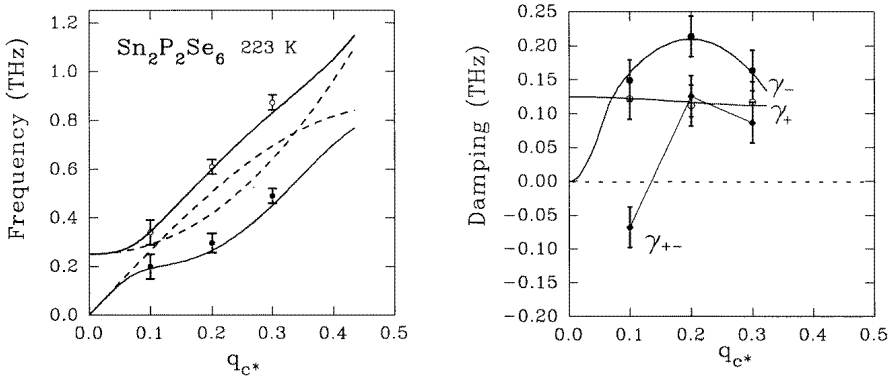

Figure 20. The dispersion at 223 K with diagonalized frequencies (ω_+ and ω_-). The dashed lines are the bare branches in the continuum model, which transform into the full lines on taking the coupling into account ($T_{\text{model}} = 205$ K).

A clear soft-mode behaviour is thus observed, in which a concave shape develops in the lower branch above 0.1 $\boldsymbol{c}^*$. The position of the inflexion point on the concave shape shifts to lower q-positions on approaching the incommensurate transition, indicating its direct relationship with the incommensurate instability at about 0.1 $\boldsymbol{c}^*$ (near T_i).

It should be noticed that the dynamics at 0.1 $\boldsymbol{c}^*$ at 223 K and 230 K will be influenced by the presence of the central peak: a coupling of the soft mode to the central peak will in general stabilize the soft-mode frequency.

4.5. The Landau model

A more direct picture of the relationship between the observed branch softening and the incommensurate transition can be obtained from a simple model for the dispersion curves and interaction strengths, valid in the low-q continuum limit.

Such a model is suggested by the analysis of the spectra with the assumption of real coupling (see figure 21, 230 K). It assumes that all of the soft-fluctuation behaviour is

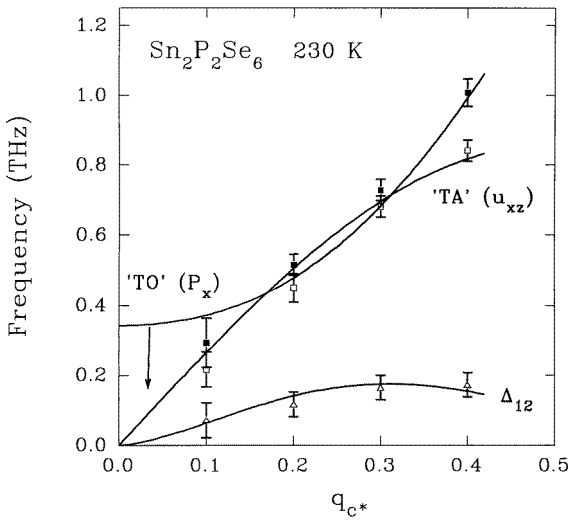

Figure 21. The dispersion at 230.7 K, $\boldsymbol{Q} = (3\ 0\ 1+\xi)$ obtained using the real coupling Δ_{12}: ■: ω_{opt} (broad mode); □: ω_{ac} (sharp mode); △: Δ_{12}. The full lines are obtained from the continuum model (see the text).

contained in a 'bare' T-dependent optic mode (polarization P_x), which interacts with a temperature-independent acoustic mode (strain u_{xz}) via a temperature-independent (and real) interaction strength $d(q) = 2\sqrt{\omega_O\omega_A}\Delta_{12}(q)$.

This is indicated in the temperature dependence of the 'bare' dispersion curves along $\boldsymbol{c}^*$, obtained under the assumption of *real* coupling (Δ_{12}). The dispersion branches, corresponding to a heavily damped (TO) phonon and a sharp (TA) phonon (section 4.3), are found to be relatively close together for all three temperatures 223 K, 230 K and 297 K. The acoustic branch stays constant within the error bars, whereas a clear softening of the damped optic branch is present upon lowering the temperature. The largest changes occur at low q_{c^*}, and are experimentally quite clear for 0.2 $\boldsymbol{c}^*$. The interaction parameter Δ_{12} clearly shows an increase along the dispersion branch, and reaches large values approaching the Brillouin zone boundary. It shows a slight increase upon lowering the temperature, related to the softening of the optic branch (figure 21), in agreement with $d(q) = 2\sqrt{\omega_O\omega_A}\Delta_{12}(q) \cong$ constant.

The observed temperature variation of the branches may be modelled by extending the thermodynamic potential of section 3, including an interaction between the polarization P_x and the strain $u_{xz} = \partial u_x/\partial z$.

In incommensurate phases of type II proper ferroelectrics (for example $NaNO_2$, thiourea and BCCD [49]), such a coupling between the strain and the order parameter coordinate (polarization) can be the origin of the incommensurate instability, as first discussed for the IC phase in quartz by Levanyuk and Aslanyan [50]. The lowest-order thermodynamic potential for $Sn_2P_2Se_6$ up to fourth order, including a $(\gamma/6)P^6$ term for stabilization of the ferroelectric phase ($\beta < 0$), is [50]

$$\Phi = \Phi_0 + \frac{\alpha}{2}P^2 + \frac{\beta}{4}P^4 + \frac{\gamma}{6}P^6 + \frac{\delta}{2}\left(\frac{\mathrm{d}P}{\mathrm{d}z}\right)^2 + \frac{g}{4}\left(\frac{\mathrm{d}^2P}{\mathrm{d}z^2}\right)^2 + \frac{\lambda}{2}P^2\left(\frac{\mathrm{d}P}{\mathrm{d}z}\right)^2 + \frac{C}{2}\left(\frac{\partial u_x}{\partial z}\right)^2 + \mu\frac{\partial u_x}{\partial z}\frac{\mathrm{d}P}{\mathrm{d}z} \tag{13}$$

in which $\partial u_x/\partial z$ is the strain u_{xz}. The interaction is represented by the last term

$$\mu \frac{\partial u_x}{\partial z} \frac{\mathrm{d}P_x}{\mathrm{d}z}.$$

If we assume travelling waves along the z-axis $P = P_q \mathrm{e}^{\mathrm{i}qz - \mathrm{i}\omega t}$, $u = u_q \mathrm{e}^{\mathrm{i}qz - \mathrm{i}\omega t}$ we arrive at the following equation for the potential:

$$\Phi(P, u, q) = \left(\frac{\alpha}{2} + \frac{\delta}{2}q^2 + \frac{g}{4}q^4\right)P_q^2 + \left(\frac{\beta}{4} + \frac{\lambda}{2}q^2\right)P_q^4 + \frac{\gamma}{6}P_q^6 + \frac{C}{2}q^2u_q^2 + \mu q^2 u_q P_q. \tag{14}$$

From this we obtain the dynamical matrix in the paraelectric phase from

$$D_{ij} = \left.\frac{\partial^2 \Phi}{\partial Q_i \, \partial Q_j}\right|_{Q_{i,j}=0}$$

in which $Q_1 = P_q$ and $Q_2 = u_q$†:

$$\mathbf{D} = \begin{pmatrix} \omega_{opt}^2 & d(q) \\ d(q) & \omega_{ac}^2 \end{pmatrix} = \begin{pmatrix} \alpha + \delta q^2 + (g/2)q^4 & \mu q^2 \\ \mu q^2 & v_A^2 q^2 \end{pmatrix}.$$

The interaction turned out to be better described by‡

$$d(q) = \frac{\mu q}{1.5\pi} \sin(1.5\pi q) \tag{15}$$

over a wider q-range, corresponding to an interaction $d(q) = \mu q^2$ for small q, in which μ was adjusted to fit the development of the interaction parameter Δ_{12} throughout the Brillouin zone (table 5).

In our model, we accounted for the effects of the discrete lattice by taking

$$\omega_A = \frac{v_A}{\pi} \sin(\pi q) \tag{16}$$

for the acoustic dispersion ω_A, according to a discrete nearest-neighbour 'single-ion' spring dispersion, and the interaction $d(q)$ as given in equation (15).

In figures 18–20 and 21 we included the analysis of the dispersion curves at 230 K and 223 K, 297 K according to this dynamical matrix. The initial parameters are given in table 5.

Table 5. Model parameters for $Sn_2P_2Se_6$.

a (THz^2 K^{-1})	T_0 (K)	δ (THz^2 $(c^*)^{-2}$)	g (THz^2 $(c^*)^{-4}$)	μ (THz^2 $(c^*)^{-1}$)	v_A (THz c^*)
0.0018	170	1.9	44	4.2	2.7

These parameter values are based as much as possible on values known from other experiments on $Sn_2P_2Se_6$. For the sound velocity v_A, the sound velocity at room temperature obtained in ultrasound measurements has been used ($v_A(xz) = 1.83 \times 10^3$ m s^{-1} at 295 K;

† The normal coordinates $Q_1 = P_q$ and $Q_2 = u_q$ are in fact only proportional to the polarization and the strain ($\propto \mathrm{i}qu_q$). Therefore, the coefficients obtained from the dispersion analysis have to be multiplied by a specific proportionality factor to obtain the coefficients of equation (14), which for P_q is essentially the (dielectric) phonon oscillator strength.

‡ The few points on the dispersion branch prohibit an accurate selection of the q-dependence of the interaction. Models which are allowed in the full Brillouin zone (e.g. $d(q) = (\mu q/2\pi)\sin(2\pi q)$ with a maximum at around 0.3 c^*, or $d(q) = (\mu/\pi^2)\sin^2(\pi q)$ with a maximum at around 0.5 c^*), show a behaviour similar to that of the present model.

$c^* = 2\pi \times 0.1469$ Å^{-1}). Furthermore, the position of the incommensurate instability ($\boldsymbol{q}_i = 0.1031 \pm 0.0005\ \boldsymbol{c}^*$) imposes a condition on the parameters δ and g, which can be obtained by putting $\omega_-(q_i) = 0$ in equation (12). Therefore, we have $\omega_{ac}^2\omega_{opt}^2(q_i) = d^2(q_i)$, which for low q (neglecting the effects of the discrete lattice on the dispersion of the interaction and the acoustic branch) is equal to

$$q_i^2 = -\left(\frac{\delta - \mu^2/v_A^2}{g}\right). \tag{17}$$

In our model, we have put all of the temperature dependence in the parameter $\alpha = a(T - T_0)$, putting all of the soft-mode behaviour in the 'optic' (P_x) fluctuations, while keeping all of the parameters of table 5 fixed in the simulation of the branches at different temperatures. We set T_0 to the value of 170 K, motivated by the extrapolation of the paraelectric temperature dependence of the inverse dielectric susceptibility at 10^9 Hz [41], showing that the virtual paraelectric–ferroelectric phase actually is first order. The value of a was adjusted to the 297 K and 230 K data, resulting in $a = 0.0018$ THz^2 K^{-1}. This is of the same order as that obtained from the temperature dependence of the zone-centre paraelectric soft mode for the $Sn_2P_2S_6$ crystal obtained by INS.

A good agreement between the simulated optic and acoustic branches and the experimental results for the broad and sharp coupled phonons, respectively, is obtained at all three temperatures. However, at 223 K (figure 20) the agreement could only be obtained allowing for a deviation from the real temperature: $T_{\text{model}} \cong 205$ K, due the influence of the central peak. At all temperatures the dispersion of the interaction Δ_{12} is well reproduced, as shown in the example of figure 21 (230 K). Furthermore, the diagonalized branches at all three temperatures (figures 18, 19 and 20) are satisfactorily modelled at the same time.

In figure 22 we show the temperature evolution of both branches obtained from the model. The upper branch softens below 0.15 $\boldsymbol{c}^*$ and stabilizes at higher q, whereas the lower branch shows a pronounced softening in the range 0.05–0.25 $\boldsymbol{c}^*$. At low temperature (curve 4: 170.15 K) a real minimum appears in the lower branch, which condenses at $\boldsymbol{q}_{IC} \cong 0.090\ \boldsymbol{c}^*$ ($T_{\text{model}} = 170.1$ K). Therefore, the model shows that the incommensurate phase may result from the softening of the P_x-fluctuations, creating an instability at an

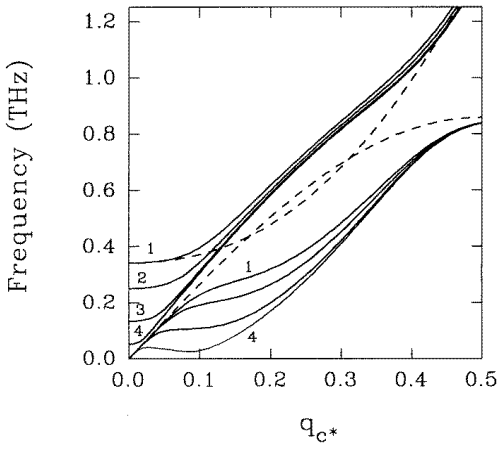

Figure 22. The model simulation of the incommensurate instability of $Sn_2P_2Se_6$. 1: 235 K; 2: 205 K; 3: 180 K; 4: 171.15 K.

incommensurate wavevector position, only because of a (constant) interaction to the hard-strain fluctuations.

It should be noted that the simulated IC phase transition occurs at too low a temperature. This may result from the presence of a central peak (figure 12), which stabilizes the soft branch at around 0.1 c^* above T_i, and contributes substantially to the inverse susceptibility χ^{-1}.

Therefore, the mixed branch does not completely condense in $Sn_2P_2Se_6$, but triggers the phase transition. Also, the few experimental points on the dispersion branch are not sufficiently numerous to allow one to model the real optic branch rigorously. Nevertheless, the present continuum model shows the importance of the observed phonon coupling for the phase transition mechanism.

It is interesting that in the present interaction model a small change in the material's parameters (such as an increase of δ and v_A, or a decrease of the interaction parameter μ) will change the position of the instability from $q_{IC} \neq 0$ to $q_C = 0$. For example, applying the parameter set given in table 6 will result in a ferroelectric phase transition rather than an incommensurate transition. In the parentheses, the borderline values for passing to a direct paraelectric–ferroelectric transition are given, starting from the parameter set of table 5, and changing one of the parameters δ, μ or v_A.

Table 6. Model parameters for a direct paraelectric–ferroelectric phase transition. In the parentheses the limiting values are given.

a (THz^2 K^{-1})	T_0 (K)	δ (THz^2 $(c^*)^{-2}$)	g (THz^2 $(c^*)^{-4}$)	μ (THz^2 $(c^*)^{-1}$)	v_A (THz c^*)
0.0018	170	2.4 (2.38)	50	4.0 (3.7)	2.7 (3.05)

The sensitivity of the reciprocal-space position of the instability to the material parameters δ, μ and v_A allows us to investigate further the origin of the Lifshitz point of the x–T phase diagram of $Sn_2P_2(S_{1-x}Se_x)_6$. For example, the sound velocity of $Sn_2P_2S_6$ is 3.24 THz c^* (with $c^* = 2\pi \times 0.1536$ Å^{-1} [13]), which exceeds the maximum value by 6% (table 6). A linear change of the sound velocity solely as function of composition would result in the disappearance of the incommensurate phase at $x = 0.35$, quite close to the actual Lifshitz composition ($x_L = 0.28$). Therefore, the interaction seems to play a substantial role in the presence of the Lifshitz point in the phase diagram. A comparative study of the dispersion properties of $Sn_2P_2S_6$ will be published in a separate paper.

4.5.1. Concluding remarks. It is interesting to speculate on the origin of the observed strong interaction. A possibility would be a relationship to the disorder of the tin atoms, recently observed in x-ray structure refinement of the paraelectric phase. The tin atoms occupy two (quasi-) equilibrium positions, separated by 0.34 Å (293 K).

It is known from microscopic modelling of the phase transitions of $NaNO_2$ by Michel and co-workers [51] that the rotational disorder of the NO_2 molecules in the paraelectric phase results in an interaction between the translational and rotational movements of the NO_2 molecules. It would be interesting to calculate the coupling strength induced by the disorder for $Sn_2P_2Se_6$.

Finally, it is important to notice that the condensed mode will be of mixed optic–elastic character rather than a pure polarization wave (the continuum model analysis suggests that the order parameter $Q_s = 0.87P_q - 0.50u_q$ close to T_i.). Therefore, the IC phase is expected to have an intrinsic elastic modulation component, as is the case for $NaNO_2$.

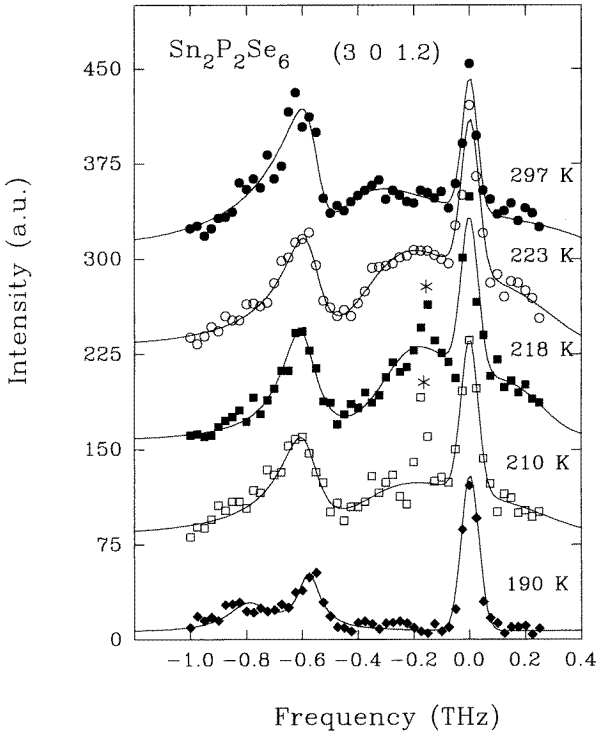

Figure 23. The temperature dependence of the spectra at $\boldsymbol{Q} = (3\ 0\ 1.2)$. The sharp peak (∗) at around 0.15 THz at 218 K and 210 K in the incommensurate phase is probably related to Bragg contamination by the nearby satellite diffraction peak. The solid lines are fits according to the CDHO model for the phonons.

This may explain the observed self-focusing of light [52] for crystals in which the incommensurate modulation wavelength is of the order of the wavelength of light ($x = 0.40$), which may be produced by the strong elastic properties of the incommensurate phase, through the photoelastic constants.

Moreover, it will be of importance in the understanding of the temperature dependence of the dielectric constant in the IC phase, which has not yet been clarified using the modulated polarization as the IC order parameter in Landau models.

4.6. The dynamics in the incommensurate phase

The temperature dependence of the soft branch across the phase transition sequence paraelectric–incommensurate–ferroelectric has been studied in most detail at (3 0 1.2) (see figure 23). In the paraelectric and incommensurate phases, clear interference line-shapes for the TO and TA phonon are observed, as analysed in the CDHO model (continuous lines). The intensity at low frequency, around 0.25 THz, increases when cooling in the paraelectric phase, and the maximum at 0.25 THz slightly shifts to lower frequencies; this is related to the soft-branch softening. At the same time, the intensity at frequencies above the sharp maximum at 0.6 THz is reduced.

In the incommensurate phase the intensity at around 0.25 THz decreases gradually, as is clearly observed by comparing the spectra at 218 K and 210 K, indicating a hardening of

the soft branch. The strong, sharp peak (∗) at around 0.15 THz at 218 K and 210 K in the incommensurate phase is probably related to Bragg contamination by the nearby satellite diffraction peak, which increases in intensity and shifts to lower values of q_{c^*} upon lowering the temperature in the IC phase. The sharp maximum may also reflect a new acoustic branch, starting at the satellite Bragg reflection. The response can hardly be related to the phason, since dielectric measurements by Grigas *et al* [19] show that the phason is at much lower frequencies. Furthermore, it can be expected to be severely overdamped.

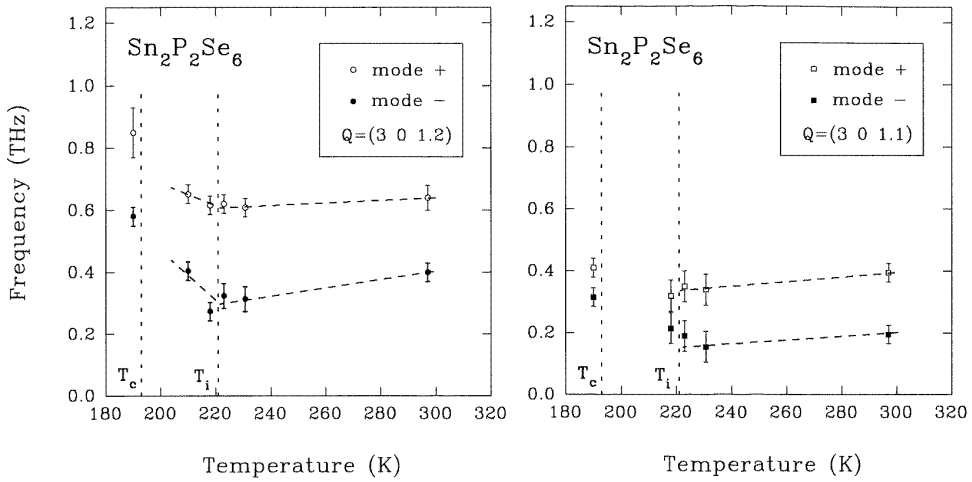

Figure 24. The temperature dependence of the diagonalized frequencies at $\boldsymbol{Q} = (3\ 0\ 1.2)$ and $\boldsymbol{Q} = (3\ 0\ 1.1)$.

In the incommensurate phase, the soft mode of the paraelectric phase is expected to split into two new excitations, the amplitudon and the phason, which correspond to fluctuations of the amplitude and phase of the incommensurate modulation displacement wave, respectively [53, 54]. We attribute the 'optic' phonon in the IC phase to the response of the branch corresponding to the amplitudon, which shows a pronounced coupling to the TA (xz) phonon and seems to harden in the incommensurate phase. This can be seen from the temperature dependence of the (diagonalized) frequency at $\boldsymbol{Q} = (3\ 0\ 1.2)$ in figure 24, where the lower branch shows a clear softening in the paraelectric phase and hardens in the incommensurate phase. The hardening is also reflected in the intensity monitored at 0.25 THz as a function of temperature (figure 25), where a gradual decrease of the intensity is observed in the incommensurate phase. Here, the anomalous peak (∗) may also contribute, prohibiting a quantitative interpretation from being made. It seems clear that a discrete change of the dynamical parameters occurs at the (first-order) lock-in transition for 0.2 $\boldsymbol{c}^*$ (figure 25).

In the ferroelectric phase at 190 K the low-frequency intensity has almost disappeared; besides a sharp peak at 0.6 THz, there is a small maximum at around 0.85 THz. The (3 0 ±1.1) data show a similar behaviour. The ferroelectric modes are found at higher frequencies than for the other phases (figure 24).

Similar phenomena can be observed in the (4 0 $\pm q_{c^*}$) and (4 0 2 + q_{c^*}) geometries (figures 13, 14 and 17). From these spectra, it can clearly be seen that the spectra do not change much upon lowering the temperature from RT down to 210 K, except minor changes, which are related to a small hardening of the amplitudon in the IC phase (0.81 THz (223 K) to 0.85 THz (210 K) at 0.4 $\boldsymbol{c}^*$), consistent with the (3 0 1.2) results and expected

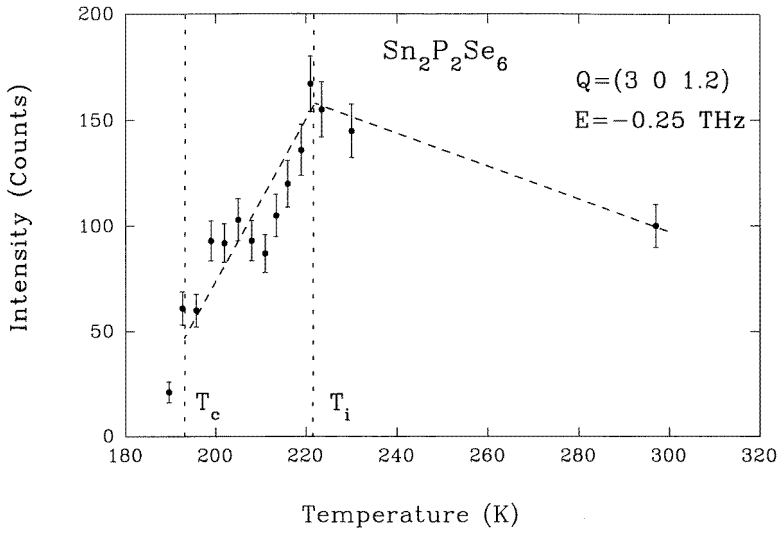

Figure 25. The temperature dependence of the intensity monitored at $E = -0.25$ THz for $\boldsymbol{Q} = (3\ 0\ 1.2)$.

Table 7. Coupled-DHO parameters for (4 0 2.4). ($\omega_{1,2}$, γ_{12}, Δ_{12} in THz, $\Delta\phi_{1,2}$ in degrees and F_1, F_2 in arbitrary units).

Q	$\lvert F_1(\boldsymbol{Q})\rvert$	$\lvert F_2(\boldsymbol{Q})\rvert$	Δ_{12}	γ_{12}	ω_1	ω_2	$\Delta\phi_{1,2}$
285 K	1.80	0.75	0.17	0.00	1.00	0.82	37
185 K	1.85	0.75	0.10	0.00	1.00	0.93	26

from simple theoretical models.

In the (4 0 2.4) (figure 17) and (4 0 1.6) spectra, the low-frequency maximum in the dynamics below 1.2 THz further reduces in intensity upon lowering the temperature to 194 K, just above T_c. The tail suddenly disappears below the lock-in transition at $T_c = 193$ K. The dynamic parameters therefore experience a discrete jump at T_c. All of the spectra at 0.4 $\boldsymbol{c}^*$ turned out to be best modelled by putting the interaction to zero ($\Delta_{12} \rightarrow 0$) immediately below the transition. Such an analysis is also satisfactory at 0.2 $\boldsymbol{c}^*$. A comparison of the (4 0 2.4) and (4 0 1.6) spectra at 186 K shows their similarity in the ferroelectric phase, and to the response at (4 0 $\pm$0.4), in contrast to the responses in the high-temperature phases. Above T_c, the (4 0 2.4) spectrum mainly reflects the response of the optic phonon, whereas the (4 0 1.6) spectrum reflects that of the acoustic phonon (section 4.3, table 4). Below T_c, the same can be expected; in the ferroelectric phase the optic and acoustic phonons are therefore at about the same frequency and cannot be separated. All of the trial interpretations following this scheme in the eight-parameter model including a strong interaction ($\Delta_{12} \geqslant 0.06$) were found to be inconsistent with the observed spectra. For example, for two coupled phonons at the same frequency, one should obtain a double-maximum structure in most cases, clearly not observed below T_c.

It should be noticed, however, that the phase factors of the structure factor in equation (11) play an important role in the exact interpretation of the dynamics. For example, the spectral shape difference for (4 0 2.4) and (4 0 $\pm$ 0.4) could only be obtained for slightly

different interaction strengths (see section 4.3, table 4). Allowing the phase to be non-zero allows one to vary the response further and a better agreement can probably be obtained (table 7). As discussed, such an analysis is however beyond the scope of the present paper.

5. Conclusions

This study shows that inelastic neutron scattering investigation gives a wealth of information about $Sn_2P_2Se_6$.

A good agreement as regards the behaviour of the satellites with previous x-ray experiments is found. A power law for the intensity is observed with $\beta = 0.43 \pm 0.03$, in agreement with NMR and birefringence results, indicating that the incommensurate phase is critical over a small temperature range only. The increase in intensity close to the lock-in phase transition resembles dilatation and birefringence results. The origin and relation to the lock-in transition is unclear, which calls for more theoretical research.

The incommensurate phase formation is shown to result from the condensation of a system of coupled TO (P_x) and TA (u_{xz}) phonons, and not through optic–optic interaction, although this is also present. Changes in the interaction parameters v_A, δ and μ upon changing the composition x may explain the presence of the Lifshitz point, at which the wavelength of the modulation becomes infinite.

The dynamics in the phase transition sequence paraelectric–incommensurate–ferroelectric can be modelled in the following scheme. In the paraelectric phase, a transverse mixed optic–acoustic soft mode polarized along the x-direction condenses at the modulation wavevector position. The transition is mainly displacive with a minor order–disorder component. In the incommensurate phase the amplitudon branch is observed. The amplitudon is coupled to the TA phonon at non-zero q_c^*, and increases in frequency upon lowering the temperature in the IC phase. At the lock-in transition, the modes show discrete changes towards higher frequencies, and a reduced interaction strength. In the ferroelectric phase a clear zone-centre soft phonon is observed, which at low temperature shows an additional coupling to the (z-polarized) optic phonon(s).

Furthermore, the phonon responses were of high intensity, and the soft phonon appears to be underdamped even quite close to the phase transition. Therefore, the study of crystals of the 'Lifshitz' composition is expected to be feasible, even though the fluctuations are expected to be stronger. A recent theory [10] predicts that the critical exponents of the Lifshitz point deviate substantially from mean-field values ($\beta = \frac{1}{3}$, $\alpha = \frac{1}{6}$ and $\gamma = 1\frac{1}{6}$). Furthermore, the expected critical range, estimated from the Levanyuk–Ginzburg criterion, is large: $\tau = 10^{-2}$–10^{-1} (between 3 K and 90 K). Therefore, the temperature behaviour of the soft phonon might be used to determine the exponent γ.

Future inelastic neutron scattering research on the properties of the mixed Pb–Sn compounds $(Pb_ySn_{1-y})_2P_2Se_6$, which show a low-temperature incommensurate phase over a broad temperature range, seems to be promising as regards studying the effect of quantum mechanical fluctuations on the dynamics.

Acknowledgments

One of us, S W H Eijt, wishes to thank the Dutch Organization for Fundamental Research on Matter (FOM) for financial support. The authors acknowledge technical support by P Boutrouille and A Brochier.

References

[1] Harada J, Axe J D and Shirane G 1971 *Phys. Rev.* B **4** 155
[2] Moudden A H, Denoyer F, Benoit J P and Fitzgerald W 1978 *Solid State Commun.* **28** 575
[3] Brill W and Ehses K-H 1985 *Japan. J. Appl. Phys. Suppl.* **24** 826
[4] Yamamoto A 1985 *Phys. Rev.* B **31** 5941
[5] Levanyuk A P and Sannikov D G 1976 *Sov. Phys.–Solid State* **18** 1122
[6] Chen Z Y and Walker M B 1990 *Phys. Rev. Lett.* **65** 1223
[7] Maior M M, Rasing Th, Eijt S W H, van Loosdrecht P H M, van Kempen H, Molnar S B, Vysochanskii Yu M and Motrij S F 1994 *J. Phys.: Condens. Matter* **6** 11 211
[8] Vysochanskii Yu M 1996 *Ferroelectrics* **183** 143
[9] Gommonai A V, Grabar A A, Vysochanskii Yu M, Belyaev A D, Machulin V F, Gurzan M I and Slivka V Yu 1981 *Fiz. Tverd. Tela* **23** 3602
[10] Folk R and Moser G 1993 *Phys. Rev.* B **47** 13 992
Nasser I and Folk R 1995 *Phys. Rev.* B **52** 15 799
Afaf Abdel-Hady and Folk R 1996 *Phys. Rev.* B **54** 3851
[11] Israel R, Eijt S W H, de Gelder R, Smits J, Beurskens P T, Rasing Th, van Kempen H, Maior M M and Motrija S F 1998 *Z. Kristallogr.* **213** 34
[12] Voroshilov Yu V, Portorii M N, Seikovskaya L A, Yatsenko A V and Prits I P 1988 *Sov. Phys.–Crystallogr.* **33** 761
[13] Dittmar G and Schaeffer H 1974 *Z. Naturf.* b **29** 312
[14] Scott F, Pressprich M, Willet R D and Cleary D A 1992 *J. Solid State Chem.* **96** 294
[15] Rizak V M, Vysochanskii Yu M, Grabar A A and Slivka V Yu 1990 *Sov. Phys.–Solid State* **31** 1185
[16] Grabar A A, Vysochanskii Yu M and Slivka V Yu 1984 *Sov. Phys.–Solid State* **26** 1859
[17] Vysochanskii Yu M, Slivka V Yu, Buturlakin A P, Gurzan M I and Chepur D V 1978 *Sov. Phys.–Solid State* **20** 49
[18] Volkov A A, Kozloc G V, Afanas'eva N I, Vysochanskii Yu M, Grabar A A and Slivka V Yu 1983 *Sov. Phys.–Solid State* **25** 1482
[19] Grigas J, Kalesinskas V, Lapinskas S and Gurzan M I 1988 *Phase Transitions* **12** 263
[20] Valevichius V D 1987 *Sov. Phys.–Solid State* **29** 3703
[21] Valevichius V D, Samulenis V I, Vysochanskii Yu M, Maior M M and Gurzan M I 1989 *Sov. Phys.–Solid State* **31** 1180
[22] Ritus A I, Rislik N S, Vysochanskii Yu M, Grabar A A and Slivka V Yu 1985 *Sov. Phys.–Solid State* **27** 1337
[23] Maior M M, Koperles B M, Savchenko B A, Gurzan M I, Morozova O V and Korda N F 1983 *Sov. Phys.–Solid State* **25** 117
[24] Gommonai A V, Vysochanskii Yu M, Gurzan M I and Slivka V Yu 1983 *Sov. Phys.–Solid State* **25** 835
[25] Eijt S W H, Maior M M and Vysochanskii Yu M 1996 *Ferroelectrics* **185** 237
[26] Barsamian T K, Khasanov S S, Shekhtman V Sh, Vysochanskii Yu M and Slivka V Yu 1986 *Sov. Phys.–Solid State* **27** 2003
[27] Barsamian T K, Khasanov S S and Shekhtman V Sh 1993 *Ferroelectrics* **138** 63
[28] Gommonai A V, Vysochanskii Yu M and Slivka V Yu 1982 *Sov. Phys.–Solid State* **24** 606
[29] Grigas J, Kalesinskas V, Lapinskas S and Paprotny W 1988 *Ferroelectrics* **80** 225
[30] Ishibashi Y and Shiba H 1978 *J. Phys. Soc. Japan* **45** 801
[31] Vysochanskii Yu M, Maior M M, Rizak V M, Slivka V Yu and Khoma M M 1989 *Sov. Phys.–JETP* **68** 782
[32] Durand D, Denoyer F, Lefur D, Currat R and Bernard L 1983 *J. Physique Lett.* **44** L207
[33] Vysochanskii Yu M, Furtsev V G, Khoma M M, Grabar A A, Gurzan M I, Maior M M, Perechinskii S I, Rizak V M and Slivka V Yu 1986 *Sov. Phys.–JETP* **64** 816
Vysochanskii Yu M and Slivka V Yu 1992 *Sov. Phys.–Usp.* **35** 123
[34] Sandler Yu M and Aleksandrov K S 1983 *Sov. Phys.–Solid State* **25** 2045
[35] Vysochanskii Yu M, Grabar A A, Dovka N D, Rizak V M, Perechinskii S I and Slivka V Yu 1991 *Izv. Akad. Nauk SSSR, Ser. Fiz.* **55** 606
[36] Maior M M, van Loosdrecht P H M, van Kempen H, Rasing Th, Molnar S B and Motrij S F 1993 *J. Phys.: Condens. Matter* **5** 6023
[37] Golovko V A 1988 *Sov. Phys.–JETP* **67** 316
[38] Bean C P and Rodbell D S 1962 *Phys. Rev.* **126** 104
[39] Eijt S W H, Currat R, Lorenzo J E, Saint-Grégoire P, Hennion B and Vysochanskii V Yu 1998 unpublished
[40] van Loosdrecht P H M, Maior M M, Molnar S B, Vysochanskii Yu M, van Bentum P J M and van Kempen

H 1993 *Phys. Rev.* B **48** 6014
[41] Maior M M, Vysochanskii Yu M, Bovtun V P, Poplavko Yu M and Koperles B M 1985 *Sov. Phys.–Solid State* **27** 765
[42] Tani K 1969 *J. Phys. Soc. Japan* **26** 93
[43] Kovalev O V 1965 *Irreducible Representations of the Space Groups* (New York: Gordon and Breach)
[44] Currat R, Buhay H, Perry C H and Quittet A M 1989 *Phys. Rev.* B **40** 10 741
[45] Hlinka J 1995 *PhD Thesis* Laboratoire Léon Brillouin CEA/Saclay
[46] Barker Jr A S and Hopfield J J 1964 *Phys. Rev.* **135** A1732
[47] Wehner R K and Steigmeier E F 1975 *RCA Rev.* **36** 70
[48] Boettger H 1980 *Introduction to the Theory of Lattice Dynamics* (Berlin: Vieweg)
[49] Hlinka J, Quilichini M and Janssen T 1994 *Ferroelectrics* **155** 257
[50] Aslanyan T A and Levanyuk A P 1979 *Solid State Commun.* **31** 547
[51] Fisez J and Michel K H 1983 *Z. Phys.* B **51** 127
[52] Furtsev V G, Salo L A, Vysochanskii Yu M and Slivka V Yu 1984 *Sov. Phys.–Solid State* **26** 1180
[53] Axe J D 1976 *Proc. Gatlinburg Neutron Scattering Conf. (Gattisburg)* (US Department of Commerce) p 353
[54] Bruce A D, Cowley R A and Murray A F 1978 *J. Phys. C: Solid State Phys.* **11** 3591